MOX-Report No. 17/2021

Balanced data assimilation with a blended numerical model

Chew, R.; Benacchio, T.; Hastermann, G.; Klein, R.

MOX, Dipartimento di Matematica
Politecnico di Milano, Via Bonardi 9 - 20133 Milano (Italy)

mox-dmat@polimi.it http://mox.polimi.it

Balanced data assimilation with a blended numerical model

Ray Chew[(1)], Tommaso Benacchio[(2)],
Gottfried Hastermann[(1)], Rupert Klein[(1)]

March 22, 2021

[(1)] FB Mathematik & Informatik
Freie Universität Berlin
Arnimallee 6, 14195 Berlin, Germany
{ray.chew,gottfried.hastermann}@fu-berlin.de
rupert.klein@math.fu-berlin.de

[(2)] MOX – Modelling and Scientific Computing
Dipartimento di Matematica, Politecnico di Milano
Piazza Leonardo da Vinci 32, 20133 Milano, Italy
tommaso.benacchio@polimi.it

Keywords: semi-implicit models; finite volume methods; hyperbolic equations; compressible flow; soundproof models; ensemble data assimilation methods.

AMS Subject Classification: 65M08, 65Z99, 76M12, 76R99, 86A10

Abstract

A challenge arising from the local Bayesian assimilation of data in an atmospheric flow simulation is the imbalances it may introduce. Fast-mode imbalances of the order of the slower dynamics can be negated by employing a blended numerical model with seamless access to the compressible and the soundproof pseudo-incompressible dynamics. Here, the blended modelling strategy by Benacchio et al. (2014) is upgraded in an advanced numerical framework and extended with a Bayesian local ensemble data assimilation method. Upon assimilation of data, the model configuration is switched to the pseudo-incompressible regime for one time-step. After that, the model configuration is switched back to the compressible model for the duration of the assimilation window. The switching between model regimes is repeated for each subsequent assimilation window. An improved blending strategy ensures that a single time-step in the pseudo-incompressible regime is sufficient to filter imbalances. This improvement is based on three innovations: (i) the association of pressure fields computed at different stages of the numerical integration with actual time levels; (ii) a conversion of pressure-related variables between the model regimes derived from low Mach number asymptotics; and (iii) a judicious selection of the pressure variables used in converting numerical model states when a switch of models occurs. Travelling vortex and bubble convection experiments show that the imbalance arising from assimilation of the momentum fields can be eliminated by using this blended model, thereby achieving balanced analysis fields. The leftover imbalance in the thermodynamics can be quantified by scale analysis.

Significance statement Weather forecasting models use a combination of physics-based algorithms and meteorological measurements. A problem with combining outputs from the model with measurements of the atmosphere is that insignificant signals may generate noise and compromise the physical soundness of weather-relevant processes. By selecting atmospheric processes through the toggling of parameters in a mixed model, we are able to filter the undesirable signals in an efficient way and retain the physical features of solutions produced by the model. This development has the potential to improve the techniques used to bring observations into models and with them the quality of weather forecasts.

1 Introduction

1.1 Motivation

Dynamical processes in the atmosphere evolve on a range of spatio-temporal scales, most comprehensively expressed by the fully compressible equations. Limit regimes, derived from the fully compressible equations by scale analysis and asymptotics, describe reduced dynamics, examples being the anelastic and pseudo-incompressible models traditionally used at small- to mesoscale, and the hydrostatic primitive equations at large to planetary scales [Pedlosky, 2013, Vallis, 2017, Klein, 2010].

In order to access the dynamics of the fully compressible equations and of its limit regimes, separate numerical schemes can be developed for each of the limiting models. However, from a computational standpoint, the error arising from the solution of different equation sets by the same numerical scheme can be smaller than the error associated with the solution of a single equation set by different numerical schemes [Smolarkiewicz and Dörnbrack, 2008, Klein, 2009].

Benacchio et al. [2014], Klein et al. [2014] and, separately, Smolarkiewicz et al. [2014] developed discretisation schemes for the compressible equations that allow access to the pseudo-incompressible model within a single numerical framework, showing equivalent results of both configurations in small- to mesoscale tests involving acoustically balanced flows. The blended analytical and numerical framework in Benacchio et al. [2014], Klein et al. [2014], within which the compressible to pseudo-incompressible transition is realized as a continuum of models controlled by an appropriate *blending parameter*, was conceptually extended to include access to hydrostatic models by Klein and Benacchio [2016]. Benacchio and Klein [2019] then proposed a numerical implementation and achieved equivalence of hydrostatic and non-hydrostatic model solutions on large scales in the absence of vertically propagating acoustic modes.

Balanced data assimilation provides a key motivation for blended numerical models. A problem with local data assimilation is the imbalance that it may induce [Lorenc, 2003]. As the assimilation procedure does not take heed of specific characteristics of a flow, such as conservation of mass, momentum, and energy, or of particular smoothness properties, the initial balance of a flow state may be destroyed by the assimilation procedure, see Neef et al. [2006] and more specifically Greybush et al. [2011], Bannister [2015] on the effects of localisation on balanced analysis fields.

Physically, local data assimilation in a compressible framework introduces imbalances through fast acoustic modes with velocity am-

plitudes that may be of the same order of magnitude as the velocities found in the slowly evolving balanced dynamics of interest, with potentially destructive effects on overall solution quality [Hohenegger and Schär, 2007]. Judicious use of a blended soundproof-compressible model can be employed to counteract this effect. Benacchio et al. [2014] and Klein et al. [2014] showed that imbalances inherent in the initial pressure fields can be effectively reduced by solving the initial time-steps of a simulation in the pseudo-incompressible regime so that, upon the subsequent transition to the compressible regime over several further time steps, the pressure field is balanced with respect to the initial velocities and potential temperature fields.

By extension of this insight, when mounting data assimilation on the numerics, the soundproof pseudo-incompressible model can be used as a filter for the fast acoustic modes arising from the assimilation procedure. After suppression of the fast modes, the remaining time-steps until the next assimilation procedure are solved with the compressible model.

Other methods of filtering imbalances include the post-analysis digital filter [e.g., Lynch and Huang, 1992]. However, repeated application of the filter may have undesirable effects on long-term dynamics [Houtekamer and Zhang, 2016]. Balance was shown to improve with the choice of localisation space [Kepert, 2009] and by allowing observations outside of a localisation radius to relax to a climatological mean [Flowerdew, 2015]. Hastermann et al. [2017] studied the effects of blending and the post-analysis penalty method in achieving balanced analysis fields for highly oscillatory systems. See also Zupanski [2009], Houtekamer and Zhang [2016] for reviews of balanced atmospheric data assimilation.

1.2 Contributions

This paper proposes balanced data assimilation using a blended numerical framework with the following advances:

- One-step blending of the pseudo-incompressible and compressible models by instantaneous switching. This is achieved by (a) accounting for the fact, revealed by a careful analysis of the numerical schemes, that Exner pressure fields computed at comparable stages within a time step correspond to different time levels in the compressible and soundproof model; (b) judiciously converting the thermodynamic variables between the compressible and sound-proof models motivated by low-Mach number asymptotic arguments; and (c) carefully selecting, based on (a) and (b), the pressure variables used in converting numer-

ical model states at the blending time interfaces. One-step blending is a sizeable improvement over Benacchio et al. [2014], who needed several intermediate time-steps for the blending procedure.

- Exploitation of the blended framework for balanced ensemble data assimilation. After each assimilation of data, a single time-step in the pseudo-incompressible model configuration is used to filter out the fast acoustic imbalance. The model configuration is then switched back to the compressible model. In the reported experiments, balanced analysis fields are obtained with blended data assimilation that are not achievable with the data assimilation schemes tested here.

The effects of data assimilation and blending on balanced solutions are investigated in numerical experiments with travelling vortices and rising thermals. In these tests, unbalanced data assimilation is shown to destroy solution quality, while the use of blending effectively recovers the structure of the solution as evaluated by comparison with runs without data assimilation. Scale analysis is used to quantify the error introduced by the assimilation of the momentum variables. The paper is structured as follows. Section 2 contains a brief introduction to data assimilation and the Kalman filters considered here. Section 3 reviews the blended numerical framework. Section 4 proposes the new blending scheme and section 5 details the results of numerical experiments. The effectiveness of the one-step blended soundproof-compressible scheme is investigated for balanced data initialisation in section 5.1 and its application towards balanced data assimilation in 5.3. Section 6 contains discussion and conclusions.

2 Data assimilation: a quick primer

Data assimilation is used in numerical weather prediction to improve forecast. Important alternatives are 4D-Var, which optimizes model states over a finite time horizon in the past before launching a new prediction, and local-in-time assimilation procedures. Here we focus on the latter, which promise higher computational efficiency but are more susceptible to the problem of imbalances addressed in this paper. Within this framework, data assimilation is done by combining a prior probability density function (pdf) represented by an ensemble of numerical model runs with real world observations to generate a posterior pdf. The hope in doing so is that the posterior pdf will lead to a forecast that is closer to the true state of the climate

or the weather than just relying only on either the observations or the model. More details on data assimilation can be found, e.g., in the textbook by Reich and Cotter [2015].

Consider $\mathbf{x}^n_{\text{truth}} \in \mathbb{R}^m$, a state vector describing the true state of the atmosphere projected onto the numerical degrees of freedom, with m the dimension of the discrete model state. Let us denote the forward-in-time numerical integration of the state vector as $\mathcal{F}(\mathbf{x})$, so that

$$\mathbf{x}^{n+1} = \mathbf{x}^n + \Delta t\, \mathcal{F}(\mathbf{x}^n) \tag{1}$$

describes our numerical time-stepping procedure, with $\mathbf{x}^n \in \mathbb{R}^m$ a numerical approximation of $\mathbf{x}$ at time-level n. Then a time-increment of $\mathbf{x}_{\text{truth}}$ reads

$$\mathbf{x}^{n+1}_{\text{truth}} = \mathbf{x}^n_{\text{truth}} + \Delta t\, \mathcal{F}(\mathbf{x}^n_{\text{truth}}) + \eta^n + \xi^n, \tag{2}$$

where, as mathematical models are approximations of real physical phenomena, η^n is the error associated with the imperfect model description of the true state and ξ^n is the truncation error due to the numerical discretisation. In reality, an exact description of the true atmospheric state is impossible. Therefore,

$$\mathbf{x}^n = \mathbf{x}^n_{\text{truth}} + \delta^n, \tag{3}$$

where δ^n is the total deviation from the true state $\mathbf{x}^n_{\text{truth}}$ comprising the accumulation of ξ^q and η^q for $(q = 1, ..., n)$ as well as uncertainties in the initial data.

With $\mathbf{x}^n_{\text{truth}}$, a way to obtain observations $\mathbf{y}^n_{\text{obs}} \in \mathbb{R}^l$ is to apply an *approximate observation operator* $\mathcal{H} : \mathbb{R}^m \mapsto \mathbb{R}^l$, given as

$$\mathbf{y}^n_{\text{obs}} = \mathcal{H}(\mathbf{x}^n_{\text{truth}}) + \epsilon^n, \tag{4}$$

where l is the dimension of the observation space, and ϵ^n encompasses the errors incurred through (i) the discrete approximation of the observation process and (ii) the projection of the true state of the atmosphere onto the numerical degrees of freedom. Applying the observation operator to $\mathbf{x}^n$ yields $\mathbf{y}^n \in \mathbb{R}^l$, the state vector in observation space, *i.e.*

$$\mathbf{y}^n = \mathcal{H}(\mathbf{x}^n). \tag{5}$$

$\mathbf{y}^n$ and $\mathbf{y}^n_{\text{obs}}$ allow the distance between the forecast from the numerical model and observations of the true atmospheric state to be quantified. This sets the stage for data assimilation.

Modern weather forecasting techniques aim to represent the uncertainty of a forecast by generating an ensemble of likely candidates

of model states. Such an ensemble can be understood as an approximate representation of a probability distribution over model states. The task of local-in-time data assimilation is then as follows. Suppose we are given the probabilistic weight of each ensemble member at a previous instance in time, *i.e.*, at the beginning of the current simulation window, together with the forward simulation states of all ensemble members at the current time, *i.e.*, at the end of the simulation window. Then the *prior probability distribution* $\mathrm{pdf}_{\mathrm{prior}}$ is represented by the model states at the new time level together with their probabilistic weights inherited from the beginning of the simulation window. Now we are to readjust the current states or the probabilistic weights of the ensemble members, at fixed time, such that the resulting *posterior probability distribution* $\mathrm{pdf}_{\mathrm{post}}$ best reflects the observations that have arrived during the simulation window.

The connection between $\mathrm{pdf}_{\mathrm{prior}}$ and $\mathrm{pdf}_{\mathrm{post}}$ can be established in a Bayesian framework. Let $\mathbf{y}_{\mathrm{obs}}$ denote the observations that have arrived during the simulation window. Then Bayes' theorem gives

$$\mathrm{pdf}_{\mathrm{post}}(\mathbf{x}) = \mathrm{pdf}(\mathbf{x}|\mathbf{y}_{\mathrm{obs}}) = \frac{\mathrm{pdf}(\mathbf{y}_{\mathrm{obs}}|\mathbf{x})}{\mathrm{pdf}(\mathbf{y}_{\mathrm{obs}})}\mathrm{pdf}_{\mathrm{prior}}(\mathbf{x}). \tag{6}$$

Here $\mathrm{pdf}(\mathbf{x}|\mathbf{y}_{\mathrm{obs}})$ is the conditional probability of state $\mathbf{x}$ given the observations $\mathbf{y}_{\mathrm{obs}}$ and $\mathrm{pdf}(\mathbf{y}_{\mathrm{obs}}|\mathbf{x})$ is the probability of observation $\mathbf{y}_{\mathrm{obs}}$ given the state $\mathbf{x}$. The right-hand side of this equation is computable given the information before the data assimilation step, noting that the best available estimate of $\mathrm{pdf}(\mathbf{y}_{\mathrm{obs}})$ is the expectation of $\mathrm{pdf}(\mathbf{y}_{\mathrm{obs}}|\mathbf{x})$ with respect to $\mathbf{x}$ under the prior probability distribution. See Wikle and Berliner [2007], Reich and Cotter [2013] for more details on Bayesian data assimilation.

The Kalman filters

Kalman filters are a family of popular Bayesian-based data assimilation methods [Kalman, 1960] that assumes Gaussian shape for all probability densities so that they can be fully characterised by their respective covariance matrices. Identifying the prior with the term *forecast* (f), and the posterior with the term *analysis* (a), the Kalman filter is

$$\begin{aligned}\mathbf{x}^a &= \mathbf{x}^f + \frac{\mathbf{B}\mathcal{H}^T}{\mathcal{H}\mathbf{B}\mathcal{H}^T + \mathbf{R}}(\mathbf{y}_{\mathrm{obs}} - \mathcal{H}(\mathbf{x}^f)) \\ &= \mathbf{x}^f + \mathbf{K}(\mathbf{y}_{\mathrm{obs}} - \mathcal{H}(\mathbf{x}^f)),\end{aligned} \tag{7}$$

where $\mathbf{B} \in \mathbb{R}^{m \times m}$ and $\mathbf{R} \in \mathbb{R}^{l \times l}$ are the covariance matrices associated with the forecast and observations, respectively. $\mathbf{K}$ is the Kalman gain, which rewards the forecast if $\mathbf{B} \ll \mathbf{R}$ and penalises it if $\mathbf{R} \ll \mathbf{B}$.

A class of Kalman filters, the ensemble Kalman filters, avoids the problem of high dimensionality by approximating the underlying probability density functions through the empirical distributions given by an ensemble of individual simulation states. Since the size of such an ensemble is typically much smaller than the state space, ensemble-based methods are often computationally more efficient than any scheme that aims to explicitly describe entire probability density functions on this space.

Specifically, for an ensemble of size K, the ensemble forecast is $\{\mathbf{x}_1^f, \ldots, \mathbf{x}_K^f\}$ and the ensemble's parametric information specifying its probability distribution is updated by

$$\bar{\mathbf{x}}^a = \bar{\mathbf{x}}^f + \mathbf{K}^{\text{ens}}(\mathbf{y}_{\text{obs}} - \mathcal{H}(\bar{\mathbf{x}}^f)), \tag{8a}$$

$$\mathbf{P}_K^a = \mathbf{P}_K^f - \mathbf{K}^{\text{ens}}\mathbf{P}_K^f, \tag{8b}$$

$$\mathbf{K}^{\text{ens}} = \frac{\mathbf{P}_K^f \mathcal{H}^T}{\mathcal{H}\mathbf{P}_K^f \mathcal{H}^T + \mathbf{R}}, \tag{8c}$$

where $\bar{\mathbf{x}}^{a/f}$ is the ensemble mean and $\mathbf{P}_K^{a/f} \in \mathbb{R}^{K \times K}$ is the covariance associated with the ensemble.

A drawback to the ensemble Kalman filter is that the covariance is determined by the spread of the ensemble and is therefore typically underestimated. However, ensemble inflation can be applied by multiplying the ensemble covariance by a constant factor larger than 1. This increases the covariance in the direction of the ensemble spread [Van Leeuwen et al., 2015].

This paper uses the local ensemble transform Kalman filter (LETKF) data assimilation method [Hunt et al., 2007]. The LETKF localises the observation covariance in such a way that observations farther away from the grid point under analysis have less influence, tapering off to zero influence for observations outside of a prescribed observation radius. The algorithm for the LETKF is provided in appendix A.

Localisation prevents spurious correlations of faraway observations while potentially reducing the complexity of the problem by making the observation covariance matrix closer to diagonal. A smooth localisation function, such as the truncated Gaussian function or the Gaspari and Cohn [1999] function, may be used.

3 The blended numerical model

3.1 Governing equations

In a rotating three-dimensional Cartesian domain, the adiabatic, dry compressible fluid flow equations for an ideal gas under gravity are:

$$\rho_t + \nabla_\parallel \cdot (\rho \mathbf{u}) + (\rho w)_z = 0, \tag{9a}$$

$$(\rho \mathbf{u})_t + \nabla_\parallel \cdot (\rho \mathbf{u} \circ \mathbf{u}) + (\rho w \mathbf{u})_z = -\left[c_p P \nabla_\parallel \pi + f \mathbf{k} \times \rho \mathbf{u}\right], \tag{9b}$$

$$(\rho w)_t + \nabla_\parallel \cdot (\rho \mathbf{u} w) + (\rho w^2)_z = -\left(c_P P \pi_z + \rho g\right), \tag{9c}$$

$$\alpha_P P_t + \nabla_\parallel \cdot (P \mathbf{u}) + (P w)_z = 0, \tag{9d}$$

where ρ is the density, $\mathbf{u} = (u, v)$ the vector of horizontal velocities and w the vertical velocity, P is the mass-weighted potential temperature and π is the Exner pressure. f is the Coriolis parameter on the horizontal (x, y)-plane, $\mathbf{k}$ a unit vector in the vertical direction and $\times$ the cross product. g is the acceleration of gravity acting in the direction of $\mathbf{k}$. $\circ$ denotes the tensor product, $\nabla_\parallel$ denotes the horizontal gradient while the subscripts t and z denote the partial derivatives with respect to time t and the vertical coordinate z. The pressure-related variables are related to the thermodynamic pressure p by the equation of state,

$$\pi = \left(\frac{p}{p_{\text{ref}}}\right)^{R/c_p}, \qquad P = \frac{p_{\text{ref}}}{R}\left(\frac{p}{p_{\text{ref}}}\right)^{c_v/c_p} = \rho\Theta, \tag{10}$$

where p_{ref} is a reference pressure, c_p and c_v are the heat capacities at constant pressure and constant volume, $R = c_p - c_v$ is the ideal gas constant, and Θ is the potential temperature. The parameter α_P tunes between the compressible and the pseudo-incompressible model. A derivation of the compressible flow equations from first principles is given in Klein et al. [2010].

Identifying χ with the inverse potential temperature

$$\chi = \frac{1}{\Theta}, \tag{11}$$

the Exner pressure and inverse potential temperature can be decomposed as

$$\pi = \bar{\pi} + \pi' \qquad \text{and} \tag{12a}$$

$$\chi = \bar{\chi} + \chi', \tag{12b}$$

where the bar denotes a hydrostatic background state dependent only on the vertical coordinate and the prime the perturbation. This

separation allows for the semi-implicit treatment of the right-hand side of (9), such that the time-steps are not constrained by the fast wave modes.
Rewriting (9) with (11) yields

$$\rho_t + \nabla_\parallel \cdot (P\mathbf{u}\chi) + (Pw\chi)_z = 0, \tag{13a}$$

$$(\rho\mathbf{u})_t + \nabla_\parallel \cdot (P\mathbf{u} \circ \chi\mathbf{u}) + (Pw\chi\mathbf{u})_z = -\left[c_p P\nabla_\parallel \pi + f\mathbf{k} \times \rho\mathbf{u}\right], \tag{13b}$$

$$(\rho w)_t + \nabla_\parallel \cdot (P\mathbf{u}\chi w) + (Pw\chi w)_z = -\left(c_p P\pi_z + \rho g\right), \tag{13c}$$

$$\alpha_P P_t + \nabla_\parallel \cdot (P\mathbf{u}) + (Pw)_z = 0. \tag{13d}$$

Using the notation of Smolarkiewicz et al. [2014] and Benacchio and Klein [2019],

$$\Psi = (\chi, \chi\mathbf{u}, \chi w, \chi'), \tag{14}$$

(13) can be written compactly as

$$(P\Psi)_t + \mathcal{A}(\Psi; P\mathbf{v}) = Q(\Psi; P), \tag{15a}$$

$$\alpha_P P_t + \nabla \cdot (P\mathbf{v}) = 0, \tag{15b}$$

where $\mathbf{v} = (u, v, w)$ subsumes the three-dimensional velocity fields, $\mathcal{A}(\Psi; P\mathbf{v})$ denotes the advection of the quantity Ψ given the advective fluxes $P\mathbf{v}$, while $Q(\Psi; P)$ describes the effect on the right-hand side of (13) on Ψ given P.

From (10), P is solely a function of π,

$$P(\pi) = \frac{p_{\text{ref}}}{R}\pi^{\frac{1}{\gamma-1}}, \tag{16}$$

where $\gamma = c_p/c_v$ is the isentropic exponent. With (16), (15b) becomes

$$\alpha_P \left(\frac{\partial P}{\partial \pi}\right) \pi_t = -\nabla \cdot (P\mathbf{v}). \tag{17}$$

3.2 Summary of the numerical scheme

Equation (13d) is discretized in time with an implicit midpoint method,

$$\alpha_P P^{n+1} = \alpha_P P^n - \Delta t\ \nabla \cdot (P\mathbf{v})^{n+1/2}. \tag{18}$$

In order to obtain the advective fluxes at the half time-level, the time-update for equations (15) is split into advective and non-advective terms. The advection terms on the left are updated by

$$(P\Psi)^{\#} = \mathcal{A}_{\text{1st}}^{\Delta t/2}\left[\Psi^n; (P\mathbf{v}^n)\right], \tag{19a}$$

$$\alpha_P P^{\#} = \alpha_P P^n - \frac{\Delta t}{2}\tilde{\nabla} \cdot (P\mathbf{v})^n, \tag{19b}$$

where $\tilde{\nabla}$ is the discrete divergence and $\mathcal{A}_{\text{1st}}$ is an advection scheme corresponding to the half time-level update. The terms on the right are then advanced using an implicit Euler method,

$$(P\Psi)^{n+1/2} = (P\Psi)^{\#} + \frac{\Delta t}{2} Q(\Psi^{n+1/2}; P^{n+1/2}), \tag{20a}$$

$$\alpha_P P^{n+1/2} = \alpha_P P^n - \frac{\Delta t}{2} \tilde{\nabla} \cdot (P\mathbf{v})^{n+1/2}. \tag{20b}$$

Expressions (19) and (20) yield the advective fluxes at the half time-level.

Subsequently, the quantities Ψ are updated to the full time-level with an explicit Euler half step followed by a full advection step and a final implicit Euler half step,

$$(P\Psi)^{*} = (P\Psi)^{n} + \frac{\Delta t}{2} Q(\Psi^{n}; P^{n}), \tag{21a}$$

$$(P\Psi)^{**} = \mathcal{A}_{\text{2nd}}^{\Delta t} \left[\Psi^{*}; (P\mathbf{v}^{n+1/2}) \right], \tag{21b}$$

$$(P\Psi)^{n+1} = (P\Psi)^{**} + \frac{\Delta t}{2} Q(\Psi^{n+1}; P^{n+1}), \tag{21c}$$

$$\alpha_P P^{n+1} = \alpha_P P^{n} - \Delta t \tilde{\nabla} \cdot (P\mathbf{v})^{n+1/2}, \tag{21d}$$

yielding a second-order accurate one-step method [Benacchio and Klein, 2019, Smolarkiewicz, 1991, Smolarkiewicz and Margolin, 1993].

A first-order Runge-Kutta method is used for the first advection operator $\mathcal{A}_{\text{1st}}^{\Delta t/2}$ in (19a) while second-order Strang splitting is used for $\mathcal{A}_{\text{2nd}}^{\Delta t}$ in (21b). The former is necessary for the time-level analysis in section 4 to hold and the latter for an overall second-order accurate in time update. The spatial discretisation of the numerical scheme is based on a finite volume framework, for more details see section 4 in Benacchio and Klein [2019].

3.3 Pseudo-incompressible regime

The switch α_P in (9) toggles access to the pseudo-incompressible model [$\alpha_P = 0$, Durran, 1989],

$$\rho_t + \nabla_{\parallel} \cdot (\rho \mathbf{v}) + (\rho w)_z = 0, \tag{22a}$$

$$(\rho \mathbf{u})_t + \nabla_{\parallel} \cdot (\rho \mathbf{u} \circ \mathbf{u}) + (\rho w \mathbf{u})_z = -\left[c_p P \nabla \pi + f \mathbf{k} \times \rho \mathbf{u} \right], \tag{22b}$$

$$(\rho w)_t + \nabla_{\parallel} \cdot (\rho \mathbf{u} w) + (\rho w^2)_z = -\left(c_p P \pi_z + \rho g \right), \tag{22c}$$

$$\nabla_{\parallel} \cdot (P\mathbf{u}) + (Pw)_z = 0. \tag{22d}$$

where (22d) enforces the sound-proof divergence constraint. See Klein [2009], Klein and Pauluis [2012], Klein and Benacchio [2016] for details of this formulation.

4 Single time-step soundproof-compressible transition

In the following, a conversion of pressure-related quantities, motivated by low Mach number asymptotics and applied prior to the model transitions, is proposed which allows for model switching within a single time-step.

4.1 Time-level of the pressure-related variables

In the simpler non-rotating case without gravity ($g,\ f = 0$), the update for the momentum equation multiplied by the potential temperature Θ in (20a) and (21c) read

$$(P\mathbf{v})_t = -c_p(P\Theta)^{\mathrm{adv}}\nabla\pi, \tag{23}$$

where the superscript *adv* denotes the quantity that becomes available after the advection substeps (19a) and (21b). Applying an implicit Euler discretisation to (23), we find

$$(P\mathbf{v})^{\mathrm{out}} = (P\mathbf{v})^{\mathrm{in}} - \delta t\, c_p(P\Theta)^{\mathrm{adv}}\tilde{\nabla}\pi^{\mathrm{out}}, \tag{24}$$

where the superscript *in* denotes the quantities at the time-level corresponding to the start of the time-step and *out* at the end. $\delta t \leq \Delta t$ is an arbitrary time-step.

4.1.1 The compressible equations

For the case $\alpha_P = 1$, using (16) a discretisation of the left-hand side of (17) yields at the half time-level

$$P^{n+1/2} - P^n = \left(\frac{\partial P}{\partial \pi}\right)^{\#}(\pi^{n+1/2} - \pi^n), \tag{25}$$

where $(\partial P/\partial\pi)^{\#}$ is obtained from P after the advection step at the half-time level, (19). Substituting (25) into (20b),

$$\left(\frac{\partial P}{\partial \pi}\right)^{\#}(\pi^{n+1/2} - \pi^n) = -\frac{\Delta t}{2}\tilde{\nabla}\cdot(P\mathbf{v})^{n+1/2}. \tag{26}$$

Identifying *out* with $n+1/2$, *in* with n and δt with $\Delta t/2$ in (24) and rearranging, (26) becomes

$$\left(\frac{\partial P}{\partial \pi}\right)^{\#} \pi^{n+1/2} - \left(\frac{\Delta t}{2}\right)^2 c_p (P\Theta)^{\#} \tilde{\nabla}\pi^{n+1/2} = \left(\frac{\partial P}{\partial \pi}\right)^{\#} \pi^{n} - \frac{\Delta t}{2}\tilde{\nabla}\cdot(P\mathbf{v})^n, \quad (27)$$

which fixes the time-level of π after the half-time step of (19) and (20) at $n+1/2$.

For the full-time stepping of (21), a similar procedure yields

$$\left(\frac{\partial P}{\partial \pi}\right)^{**} \pi^{n+1} - (\Delta t)^2 c_p (P\Theta)^{**} \tilde{\nabla}\pi^{n+1} = \left(\frac{\partial P}{\partial \pi}\right)^{**} \pi^{n} - \Delta t\tilde{\nabla}\cdot(P\mathbf{v})^n. \quad (28)$$

From (27), π is at time-level $n+1/2$ after the half-time stepping (20) while (28) starts with π at time-level n for the full-time stepping (21). Therefore, the time-level of π has to be reset from $n+1/2$ to n after the half-time step (20) and before the full time-step (21). Furthermore, the time-level of π after the full time-step (21) is $n+1$ as intended.

4.1.2 The pseudo-incompressible equations

For $\alpha_P = 0$, the coupling between P and π in (17) no longer holds and the two variables decouple, leading to

$$\nabla\cdot(P\mathbf{v}) = 0. \quad (29)$$

Enforcing this divergence constraint for the left-hand side of (24), we obtain

$$\tilde{\nabla}\cdot(P\mathbf{v})^{\text{in}} = \tilde{\nabla}\cdot\left(\delta t\, c_p (P\Theta)^{\text{adv}}\tilde{\nabla}\pi^{\text{out}}\right). \quad (30)$$

At the half-time level, $(P\mathbf{v})^{\text{in}}$ is the solution of (19) comprising the half time-step advection. Therefore,

$$\tilde{\nabla}\cdot(P\mathbf{v})^{\text{in}} = \tilde{\nabla}\cdot\left[(P\mathbf{v})^n + \frac{\Delta t}{2}\tilde{\partial}_t (P\mathbf{v})^{\#}\right], \quad (31)$$

where $\tilde{\partial}_t$ is the discrete partial time derivative. Assuming that the divergence constraint (29) has been satisfied at the end of time-step $(n-1)$, the first term on the right-hand side vanishes. As the second

term is generated by (19) starting at time-level n, *i.e.*, by an explicit advection step associated with the left-hand side of (13b) and (13c) multiplied by Θ,

$$\tilde{\partial}_t (P\mathbf{v})^{\#} + \tilde{\nabla} \cdot (P\mathbf{v} \cdot \mathbf{v})^n = 0, \tag{32}$$

equation (31) becomes

$$\tilde{\nabla} \cdot (P\mathbf{v})^{\text{in}} = -\frac{\Delta t}{2} \tilde{\nabla} \cdot \left[\tilde{\nabla} \cdot (P\mathbf{v} \circ \mathbf{v})^n \right]. \tag{33}$$

Inserting (33) back into (30), with $\delta t = \Delta t/2$ and adv as $\#$,

$$\tilde{\nabla} \cdot \left(\frac{\Delta t}{2} c_p (P\Theta)^{\#} \tilde{\nabla} \pi^n \right) = -\frac{\Delta t}{2} \tilde{\nabla} \cdot \tilde{\nabla} \cdot (P\mathbf{v} \circ \mathbf{v})^n, \tag{34}$$

where the right-hand side has fixed the time-level of π^{out} at n.

For the full time-stepping, $(P\mathbf{v})^{\text{in}}$ is the solution of (21b) and so (30) is

$$\tilde{\nabla} \cdot (P\mathbf{v})^{**} = \tilde{\nabla} \cdot \left(\frac{\Delta t}{2} c_p (P\Theta)^{**} \tilde{\nabla} \pi^{\text{out}} \right), \tag{35}$$

with

$$\tilde{\nabla} \cdot (P\mathbf{v})^{**} = \tilde{\nabla} \cdot \left[(P\mathbf{v})^n - \frac{\Delta t}{2} c_p (P\Theta)^{\#} \tilde{\nabla} \pi^n + \Delta t \, \tilde{\partial}_t (P\mathbf{v})^{**} \right], \tag{36}$$

where the second term in the square brackets is a correction of $(P\mathbf{v})$ from the implicit substep at the half time-level (20) and the third term is the solution of the advection substep at the full time-level. Assuming again that the divergence constraint (29) has been fulfilled at the onset,

$$\tilde{\nabla} \cdot (P\mathbf{v})^n = 0 \tag{37}$$

. Substitute (34) into (36),

$$\tilde{\nabla} \cdot (P\mathbf{v})^{**} = \tilde{\nabla} \cdot \left[\frac{\Delta t}{2} \tilde{\nabla} \cdot (P\mathbf{v} \circ \mathbf{v})^n + \Delta t \tilde{\partial}_t (P\mathbf{v})^{**} \right], \tag{38}$$

and note that advection substep (21b) solves the left-hand side of (13b) and (13c) multiplied with Θ, i.e,

$$\tilde{\partial}_t (P\mathbf{v})^{**} + \tilde{\nabla} \cdot (P\mathbf{v} \circ \mathbf{v})^{n+1/2} = 0, \tag{39}$$

where the half time-level of the second term emerges from the solution of substep (21a) and (21b) under the advecting fluxes $(P\mathbf{v})^{n+1/2}$. Putting (38) and (39) together yields, after re-elaborations,

$$\tilde{\nabla} \cdot (P\mathbf{v})^{**} = -\frac{\Delta t}{2} \left[1 + \frac{\Delta t}{2} \tilde{\partial}_t \right] \tilde{\nabla} \cdot \left[\tilde{\nabla} \cdot (P\mathbf{v} \circ \mathbf{v})^{n+1/2} \right]. \tag{40}$$

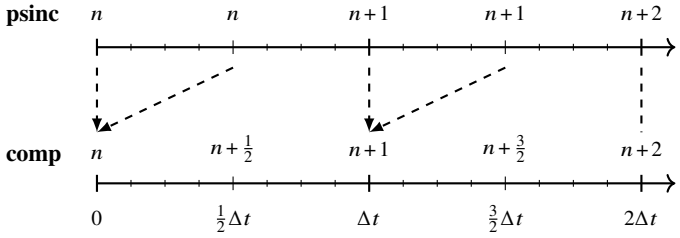

Figure 1: Summary of the time-levels of π for the pseudo-incompressible (**psinc**) and the compressible (**comp**) solutions in the numerical scheme. Δt indicates time-step size. The dashed lines relate the π's at the same time-level between the two models. The two valid choices of π in the pseudo-incompressible to compressible blending, at time t^n and t^{n+1}, are depicted with arrows.

Inserting (40) back into (35) gives

$$\tilde{\nabla}\cdot\left(c_p(P\Theta)^{**}\tilde{\nabla}\pi^{n+1}\right) = -\left(1+\frac{\Delta t}{2}\tilde{\partial}_t\right)\tilde{\nabla}\cdot\left[\tilde{\nabla}\cdot(P\mathbf{v}\circ\mathbf{v})^{n+1/2}\right], \tag{41}$$

fixing the time-level of π^{out} at $n+1$, since the right-hand side is a half time-step advancement from the $n+1/2$ time-level.

In contrast to the compressible case, expressions (34) and (41) imply that Exner pressure π after the half-step (19) is at the time-level n, and should be used as the input to (21). Here, π must not be reset to time-level n for the pseudo-incompressible solve. Figure 1 summarises the time-level analysis of π.

4.2 Conversion of the pressure-related variables

Expression (12a) separates the background Exner pressure from its perturbation. For low Mach number flows, $\text{Ma} \ll 1$, such a separation is naturally induced by the asymptotic expansion

$$\pi = \pi^{(0)} + \text{Ma}^2\pi^{(1)} + \dots\ , \tag{42}$$

where $\text{Ma} = u_{\text{ref}}/c_{\text{ref}}$ for reference velocity u_{ref} and speed of sound c_{ref}. Substituting this expansion into (17) yields

$$\alpha_P\left(\frac{\partial P}{\partial\pi}\right)\text{Ma}^2\pi_t^{(1)} = -\nabla\cdot(P\mathbf{v})\,, \tag{43}$$

based on which we can blend the pseudo-incompressible ($\alpha_P = 0$) and compressible ($\alpha_P = 1$) models. Using (16), the compressible

P_{comp} is obtained from the pseudo-incompressible model variables as

$$P_{\text{comp}} = \left(P_{\text{psinc}}^{\gamma-1} + \text{Ma}^2 \delta\pi_{\text{psinc}}\right)^{\frac{1}{\gamma-1}} . \tag{44}$$

$\delta\pi$ represents the quantity π with its mean subtracted, as π is the solution of a Helmholtz-like equation that is determinable up to a shift in its mean [eqs. (27) and (28) in Benacchio and Klein, 2019].

By inverting (44), the pseudo-incompressible P_{psinc} is obtained as

$$P_{\text{psinc}} = \left(P_{\text{comp}}^{\gamma-1} - \text{Ma}^2 \delta\pi_{\text{comp}}\right)^{\frac{1}{\gamma-1}} . \tag{45}$$

Therefore, at the blending time interfaces between the compressible and the pseudo-incompressible configurations, expression (44) or (45) is applied depending on the direction of the transition.

4.3 Association of perturbation variables between the compressible and soundproof models

The time-level analysis of π in section 4.1 demonstrated that, in a pseudo-incompressible solve, both the Exner pressure solution after the full time-step from t^n to t^{n+1} and that obtained after the *subsequent* half time-step are associated with the same time-level t^{n+1}.

Consider then the compressible to pseudo-incompressible transition at time $n+1$. P_{psinc}^{n+1} is obtained by inserting π_{comp}^{n+1} into the right-hand side of (45). Moreover, there are two valid choices for π in a pseudo-incompressible to compressible transition (Figure 1): (1) π_{full}, *i.e.*, π obtained after the full n-to-$n+1$ time step; or (2) π_{half}, *i.e.*, π obtained after the $n+1$-to-$n+3/2$ half time-step.

Choice (2) yields blended solutions that are slightly closer to the balanced solution compared to choice (1). π_{half} is obtained from the solution of the (20) with the solution of (19) as its input. The input to (19) are Ψ^n and $(P\mathbf{v})^n$. This means that π_{half} is recovered from the other quantities and is independent of π at the previous time-level, so errors in the initialisation of π are not propagated. By contrast, π_{full} is obtained from the solution of (21). The explicit (21a) has π as an input to the right-hand side $Q(\Psi^n; P^n)$. Therefore, π_{full} propagates errors in the initialisation of π. Note that choice (2) entails solving an additional time-step in the pseudo-incompressible regime to obtain π_{half}.

In addition, choice (2) offers a conceptual advantage. The Exner pressure field in the pseudo-incompressible model is not controlled

by an evolution equation but rather acts as a Lagrangian multiplier ensuring compliance of the velocity field with the divergence constraint. Thus, a direct dependence of the pressure on its previous time level data, as occurs under option (1), is a numerical artefact that should be avoided.

4.4 Data assimilation and blending

A data assimilation engine is used to insert observations in the fully compressible configuration of the blended numerical framework. Prior to the assimilation procedure at time t^n, the forecast ensemble state vector $\{\mathbf{x}_k^f\}^n$ for $k = 1, \ldots, K$ and a set of observations $\mathbf{y}_{\text{obs}}^n$ are available. K is the ensemble size. For vertical slice simulations with the compressible flow equations, the ensemble state vector is

$$\{\mathbf{x}_1^f, \ldots \mathbf{x}_K^f\}^n = \{\rho, \rho u, \rho w, P, \pi\}_{k=1,\ldots,K}^n \in \mathbb{R}^{m \times K}. \tag{46}$$

Here, the two-dimensional spatial grid has $(N_x \times N_z)$ cells and $m = (5 \times N_x \times N_z)$. The observations of the momentum fields are

$$\mathbf{y}_{\text{obs}}^n = \{(\rho u)_{\text{obs}}, (\rho w)_{\text{obs}}\}^n \in \mathbb{R}^l, \tag{47}$$

where the subscript *obs* indicates that the data is obtained externally and is noisy and sparse, and $l = (2 \times N_{\text{obs}}(n))$, with $N_{\text{obs}}(n)$ the time-dependent dimension of the sparse observation space. The observation covariance $\mathbf{R}^n$ is determined by the observation noise.

The forward observation operator $\mathcal{H}$ selects for each $\{\mathbf{x}_k^f\}^n$ in (46) the momenta $(\rho u)^n$ and $(\rho w)^n$ on the grid points corresponding to the sparse observations, thereby projecting $\mathbf{x}_k^{f,n}$ from the state space $\mathbb{R}^m$ into observation space $\mathbb{R}^l$, *i.e.*

$$\mathbf{y}_k^{f,n} = \mathcal{H}(\mathbf{x}_k^{f,n}) \in \mathbb{R}^l, \qquad k = 1, \ldots, K. \tag{48}$$

The ensemble mean in observation space is computed as

$$\bar{\mathbf{y}}^{f,n} = \frac{1}{K} \sum_{k=1}^{K} \mathbf{y}_k^{f,n} \in \mathbb{R}^l. \tag{49}$$

A similar ensemble averaging is applied to obtain $\bar{\mathbf{x}}^{f,n}$. As observation localisation is used in the LETKF algorithm [Hunt et al., 2007], only observations in a local region surrounding a given grid point are involved in its update. A localisation function is furthermore applied to the observations in the local region.

A Kalman gain $\mathbf{K}^n$ similar to (8c) is obtained from the observation operator $\mathcal{H}$, the observation covariance $\mathbf{R}^n$, and an ensemble inflation

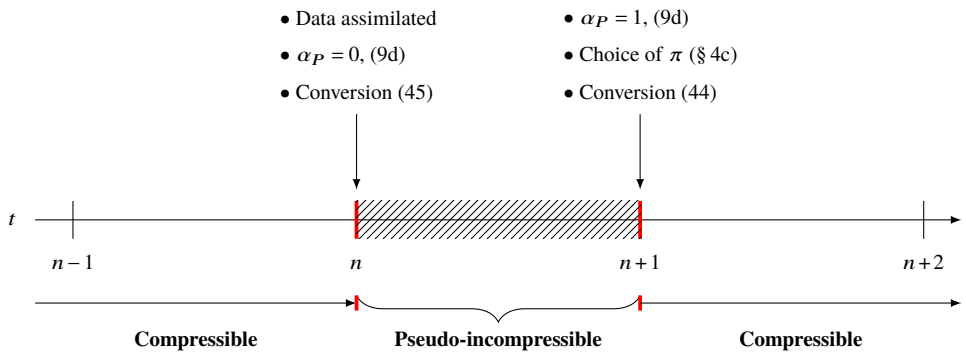

Figure 2: Schematic of data assimilation with blending for data assimilated at time t^n. Blending time interfaces are in red, and the time-step spent in the pseudo-incompressible regime is shaded. See main text for full description.

factor b. As in the right-hand side of (8a), the distance of the forecast ensemble mean from the observations is computed with (47) and (49). From these, a set of K weight vectors $\{\mathbf{w}_k^a\}^n$ is obtained, applied to (46), and added to $\bar{\mathbf{x}}^{f,n}$, updating the forecast ensemble to the analysis ensemble. Further details are given in appendix A.

Once the assimilation procedure is completed, the model switches to the pseudo-incompressible limit regime and then back again to fully compressible until the next assimilation time. This process of switching back and forth between the model configurations exploits the blended numerical model to achieve balanced data assimilation and is termed *blended data assimilation*.

In particular, if data are assimilated into the compressible flow equations at time n, then compressible to pseudo-incompressible blending entails setting the switch α_P to 0 and converting the quantity P_{comp} with (45). The solution is then propagated in the pseudo-incompressible regime for a time-step, after which α_P is set back to 1, switching to the compressible flow equations. The quantity P_{psinc} is reconverted by (44) using either π_{half} or π_{full}. Figure 2 summarises the procedure. Following the analysis from section 4.1, the perturbation variable π is reset after the half time-stepping in the solution of the full model, but not in the solution of the limit model. While additional time-steps in the pseudo-incompressible regime tend to further improve balance, numerical results suggest that a single blending time-step is sufficient. The blended data assimilation workflow is displayed in Figure 3.

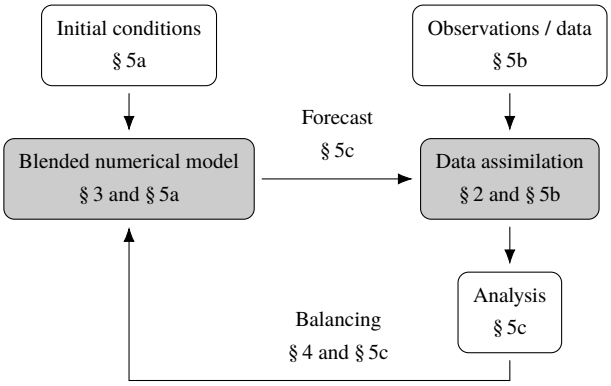

Figure 3: Blended data assimilation workflow with the sections (§) of this paper describing the algorithmic components.

5 Numerical results

The test cases of a travelling vortex and a rising warm air bubble are used to validate model performance in this section. To evaluate the effectiveness of the single time-step blended soundproof-compressible scheme, unbalanced states are initialised in the compressible flow equations for both test cases and the blended scheme is applied. The balance of the compressible solution with unbalanced initial states is evaluated by probe measurements and compared against the soundproof solution.

For blended ensemble data assimilation, an ensemble is generated by perturbing the initial conditions and the blended scheme is applied after the assimilation of observations into the compressible flow equations. This blending is repeated after each assimilation procedure. The quality of balanced data assimilation is evaluated by root mean square errors with respect to a reference solution pseudo-incompressible solution.

5.1 Effectiveness of the improved blending strategy

5.1.1 The travelling vortex experiment

The travelling vortex test case of Kadioglu et al. [2008] with $f = 0.0$ s^{-1} and $g = 0.0$ m s^{-2} is considered in the doubly periodic boundary domain $x = [-5.0\text{ km}, 5.0\text{ km}]$, $z = [-5.0\text{ km}, 5.0\text{ km}]$ with a background wind with velocity 100 m s^{-1} in both directions (Figure 4). The time-step size is constrained by advective CFL $= \|\mathbf{u}\|\Delta t/\Delta x = 0.45$ on a (64×64) grid. The choice of reference units

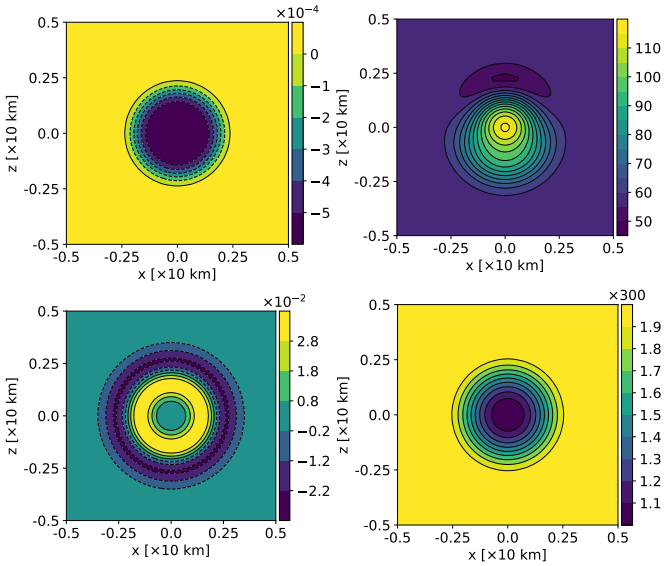

Figure 4: Travelling vortex initial balanced states: Exner pressure perturbation π; dimensionless contours in the range $[-5, 0] \times 10^{-4}$ with interval of 10^{-4} (top left), horizontal momentum ρu; contours in the range $[50, 115]$ kg m^{-1} s^{-1} with a 5 kg m^{-1} s^{-1} interval (top right), vorticity; contours in the range $[-2.2, 2.8] \times 10^{-2}$ s^{-1} with a 1.0 $\times 10^{-2}$ s^{-1} interval (bottom left), and potential temperature Θ; contours in the range $[1.1, 1.9] \times 300$ K with a 0.1×300 K interval (bottom right). Negative contours dashed.

yield Ma ≈ 0.341. Note, however, that while the background wind Mach number is relatively large, the superimposed vortex has a maximum flow velocity of 25 m s^{-1} with $\mathrm{Ma}_{\mathrm{vort}} = 0.076$, so that the low-Mach number analysis of section 44.2 is justified.

In order to gauge the performance of the improved blended model, probe measurements of the pressure perturbation increments $\delta p'$ are taken, defined, e.g. at time-level n, as

$$\delta p'^{\,n} = p'^{\,n+1} - p'^{\,n}. \tag{50}$$

at the center (0.0 km, 0.0 km). The first increment $\delta p'^{\,0}$ corresponds to a spinup adjustment and is therefore omitted in the plots, as done in Benacchio et al. [2014].

The distance in the pressure perturbation result of a run compared to the reference pseudo-incompressible run is quantified by the relative error E_ν,

$$E_\nu = \frac{\|\delta p'_\nu - \delta p'_{\mathrm{psinc}}\|_2}{\|\delta p'_{\mathrm{psinc}}\|_2}, \tag{51}$$

where ν = b for the blended run and ν = c for the imbalanced compressible run. $\|\cdot\|_2$ is the 2-norm taken over the probe measured time series of $\delta p'$.

Initial imbalanced states are created by setting $P = 10^5$ Pa and $\pi = 0.0$ over the whole domain for the compressible flow equations (21) with $\alpha_P = 1$. The initial imbalanced state is solved for one time-step in the limit pseudo-incompressible regime followed by the rest of the time-steps in the fully compressible model. The blending scheme in section 4 is used to transition between the model regimes.

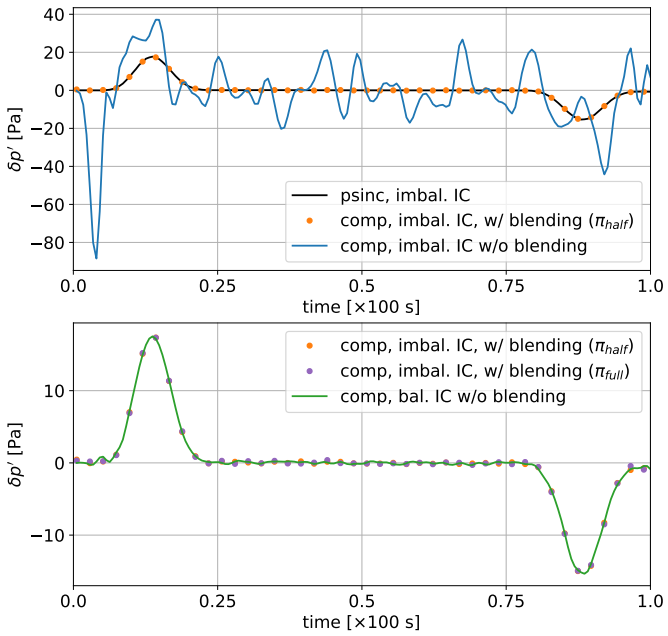

Figure 5: Travelling vortex: effect of blending for imbalanced initial states, probe measured time series of pressure perturbation increment. Top: comparison between a blended run using π_{half} (orange), a run without blending (blue), and the reference solution from the pseudo-incompressible model (black). Bottom: comparison of blended runs using π_{half} (orange) and π_{full} (purple), and the compressible solution with balanced initial states (green). The blended runs are with one time-step spent in the pseudo-incompressible regime.

For these imbalanced initial states, a compressible run with blending is compared with one without blending and with a pseudo-incompressible run (top panel in Figure 5). Fast acoustic modes are filtered from the blended solution and the result is indistinguishable from the limit pseudo-incompressible reference solution, save for an initial adjustment in the first time-step. Blending is able to recover the dynamics of the balanced state.

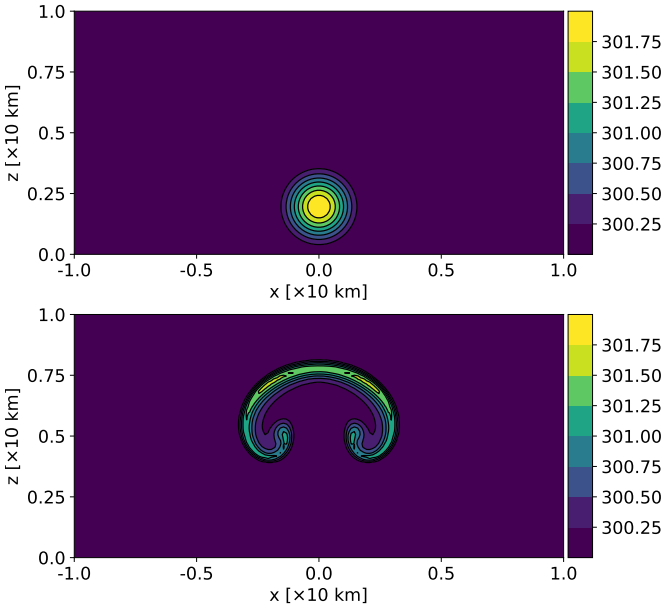

Figure 6: Rising bubble: potential temperature at initial time, $t = 0$ s and final time $t_{\text{fin}} = 1000$ s; contours in the range $[300.25, 301.75]$ K with a 0.25 K interval.

A close-up (bottom panel of Figure 5) compares the blended runs with choices of π_{half} and π_{full} from section 4.3 against a run with the balanced initial state obtained from the known exact compressible vortex solution. The blended runs are as good as, and the π_{half} run slightly closer to, the balanced compressible run. The relative error of the blended run with respect to the reference balanced run is 0.0283 using π_{half} and 0.0394 using π_{full}. This corroborates the insight from section 4.3 that π_{half} is a better choice. The choice of π_{half} is used from here on.

5.1.2 The rising bubble experiment

The second test consists of a gravity-driven thermal flow with $f = 0.0$ s^{-1} initialised as a bubble-shaped positive potential temperature perturbation $\delta\Theta$, on a constant isentropic background with $\Theta_0 = 300$ K in a $[-10.0 \text{ km}, 10.0 \text{ km}] \times [0.0 \text{ km}, 10.0 \text{ km}]$ domain, with periodic boundaries in x and no-flux in z [Benacchio et al., 2014]. The dimensionless perturbation $\delta\Theta$ is defined by

$$\delta\Theta = \frac{2\,\text{K}}{\Theta_0} \cos\left(\frac{\pi}{2} r\right), \tag{52}$$

where

$$r = \frac{1}{r_0}\sqrt{x^2 + (z - z_0)^2}, \tag{53}$$

$r_0 = 2.0$ km is the initial radius of the bubble, and $z_0 = 2.0$ km the initial vertical displacement of the bubble. The choice of reference units yields Ma ≈ 0.0341. The models are run on a grid with (160×80) cells to a final simulation time of 1000.0 s.

The initial pressure fields are set to reflect a horizontally homogeneous hydrostatic pressure field $\overline{p}(z)$ based on Θ_0 and initial condition $\overline{p}(0) = 10^5\,\mathrm{Pa}$, with $\delta\pi \equiv 0.0$. These pressure data are imbalanced, however, with respect to the perturbed initial potential temperature $\Theta_0 + \delta\Theta$, see (52). Potential temperature at the initial and final time are depicted in Figure 6.

The initial stages of the bubble evolution are compared for the compressible, pseudo-incompressible and improved blended runs in Figure 7. As the initial state is not hydrostatically balanced, pressure waves propagate in the compressible configuration (top left panel) as seen in a time series of pressure perturbation increment at $(x, z) = (-7.5, 5)$ km (orange cross in the top left panel and top right panel, blue line). The acoustics are absent in the soundproof configuration (top right panel, black line) and in the single time-step blended soundproof-compressible configuration (orange dots).

Next, the blended run and the pseudo-incompressible run are compared in more detail (Figure 7, middle and bottom panels) with pressure perturbation increment probe measurements at $(x, z) = (-7.5, 5)$ km (middle panels) and at $(x, z) = (0, 5)$ km (red cross in the top left panel and bottom panels in Figure 7), both with a constant small time-step $\Delta t = 1.9$ s (top, middle left and bottom left panels) and for larger, advective CFL-constrained time-steps (middle right and bottom right panels, CFL $= 0.5$ and $\Delta t = 21.69$ s for the first two time-steps). Away from the bubble trajectory (middle panels), the pressure perturbation increment due to the rising bubble and the remnants of the background acoustics from blending are comparable in amplitude. Larger amplitudes are observed with the blended model and the larger time step (middle right panel), but they are still very small compared to the fully compressible run (note the different range on the vertical axes between the top right and middle right panels). On the bubble trajectory (bottom panels), the pressure perturbation increment due to the rising bubble dominates and the solutions are almost identical.

Throughout the runs, a single time-step spent in the soundproof pseudo-incompressible regime largely filters out the fast acoustic imbalances of the compressible run (not shown in the middle and bottom panels of Figure 7). This is quantified by comparing the relative errors with respect to the reference pseudo-incompressible run for the compressible run, E_c, and for the blended run, E_b, defined

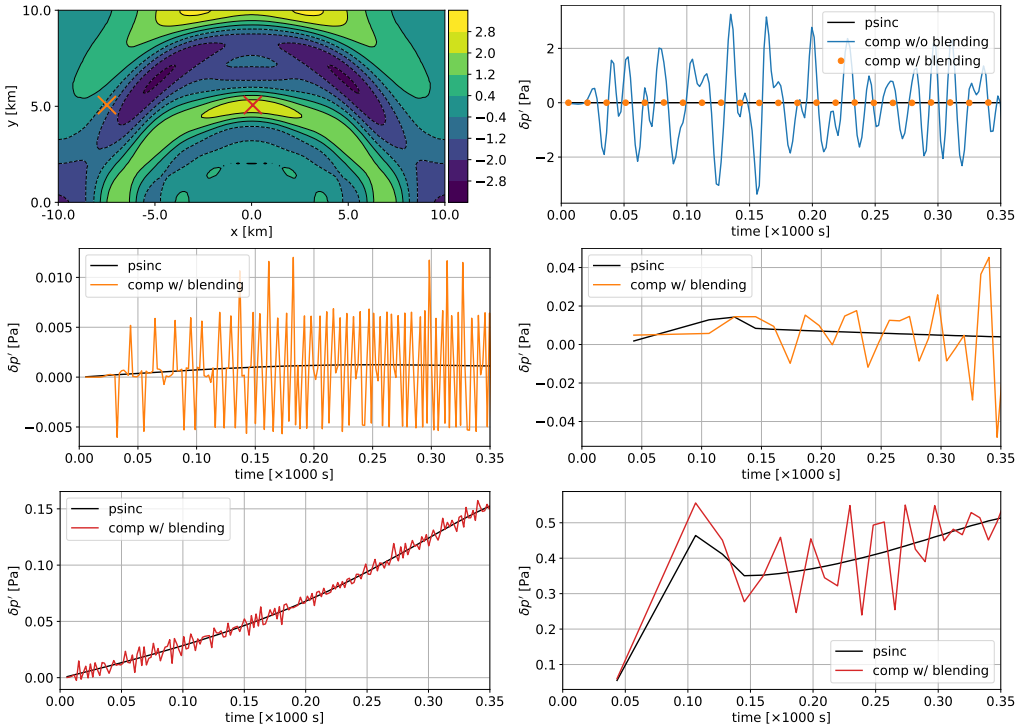

Figure 7: Time increments $\delta p'$ of pressure perturbation in the rising bubble experiment. Top left: $\delta p'$ value at time-step 14 ($t = 26.6$ s) for the compressible model; contours in the range $[-2.8, 2.8]$ Pa with an interval of 0.8 Pa, negative contours dashed. The orange cross marks $(x, z) = (-7.5, 5)$ km and the red cross $(x, z) = (0, 5)$ km. Top right: history of $\delta p'$ over the first 350 s measured at $(x, z) = (-7.5, 5)$ km for the compressible model (blue), the pseudo-incompressible model (black) and the blended model with one pseudo-incompressible time-step (orange). Middle and bottom panels: history of $\delta p'$ over the first 350 s measured at $(x, z) = (-7.5, 5)$ km (middle) and at $(x, z) = (0, 5)$ km (bottom). Pseudo-incompressible solution (black) and blended solution with one time-step spent in the pseudo-incompressible regime (orange or red corresponding to the probe marker in the top left panel). The top, middle left, and bottom left panels use a constant time-step $\Delta t = 1.9$ s. The middle right and bottom right panels use $\Delta t = 21.69$ s for the first two time-steps and then a Δt determined by advective CFL $= 0.5$.

in (51) and shown in Table 1. E_b is more than 25 times smaller than E_c for the large time-step case, and more than two orders of magnitude smaller for the small time-step case.

These results show that blending can be employed as an effective means to achieve the balanced initialisation of data within a fully compressible model. The single time-step balancing capability in

Table 1: Errors E_c and E_b (see text for definitions) of the time series of $\delta p'$ in [0, 1000] s relative to the reference pseudo-incompressible run (middle and bottom panels of Figure 7). $\Delta t_{AC} = 1.9$ s, Δt_{ADV} is determined by advective CFL = 0.5 and $\Delta t_{ADV} = 21.69$ s for the first two time-steps. Probe location $(-7.5, 5)$ km corresponds to the orange marker and orange lines in Figure 7 and $(0, 5)$ km to the red markers and red lines.

probe location	Δt	E_c	E_b	E_c/E_b
$(-7.5, 5)$ km	Δt_{AC}	413.1885	1.4804	279.11
	Δt_{ADV}	109.7538	3.9642	27.69
$(0, 5)$ km	Δt_{AC}	10.1836	0.0293	347.56
	Δt_{ADV}	2.8241	0.1012	27.91

the model presented here substantially improves on the performance of Klein et al. [2014] and Benacchio et al. [2014], whose blended models achieved smaller reductions in amplitude compared to the fully compressible case and needed several time steps in the limit regime.

5.2 Ensemble data assimilation and blending: setup

5.2.1 Travelling vortex setup

To combine blending with data assimilation as described in Section 4d, an ensemble is generated by perturbing the initial vortex center position (x_c, z_c) within the open half interval of $[-1.0 \text{ km}, 1.0 \text{ km})$ for both x_c and z_c. The vortex is then generated around this center position such that the full vortex structure is translated. Ten such samples are drawn and they constitute the ensemble members. An additional sample is drawn and solved with the full model for the balanced initial condition. This run, denoted by *obs*, is used to generate the artificial observations. Another run identical to this additional obs sample is made. This time, blending for the first time-step is applied and is considered the *truth* in the sequel. This is to correct for any errors in the initialisation of π, as discussed in section 4.3.

This choice of generating the truth and obs through a perturbation of the initial condition is such that the ensemble mean does not coincide with the truth. Otherwise, ensemble deflation alone is sufficient to make the ensemble converge towards the truth, see also Lang et al. [2017].

The observations are taken from the obs run every 25 s – only a tenth of the grid points are observed and these are drawn randomly. This deviates from a more realistic situation where observations and grid points do not coincide. To simulate measurement noise, Gaussian noise with standard deviation equal to 5% of the peak-to-peak amplitude of the obs quantity at the given time is added independently to each of the observed grid points. A similar method of generating artificial observations was used in, for example, Bocquet [2011], Harlim and Hunt [2005] for the Lorenz-63 and Lorenz-96 models.

The regions for localized data assimilation are of size (11×11) grid points and only observations within such a patch are considered for analysis operations at the respective central grid point. A localisation function corresponding to a truncated Gaussian function is applied such that observations farther from the grid point under analysis have less influence, and that the influence decays smoothly to zero towards the edges of the localization subdomain. No ensemble inflation is applied in this case.

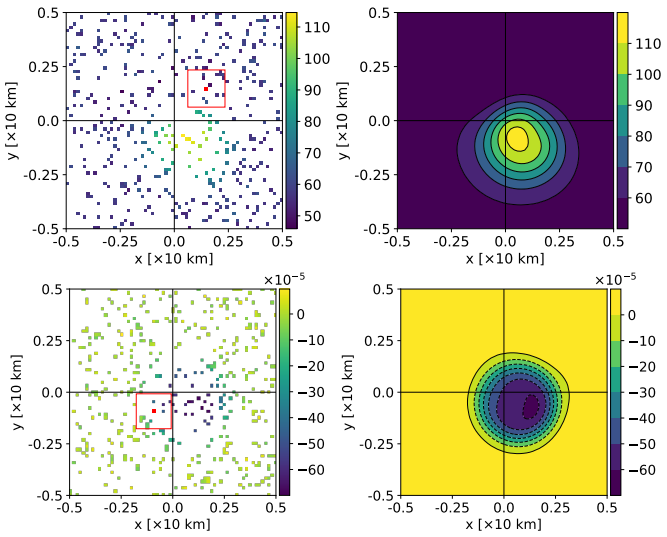

Figure 8: Travelling vortex: sparse noisy observations (left panels) and truths (right panels) at $t = 300.0$ s. Top: horizontal momentum ρu; contours in range $[60, 110]$ kg m^{-1} s^{-1} with a 10 kg m^{-1} s^{-1} interval. Bottom: Exner pressure perturbation π; dimensionless contours in range $[-60, 0] \times 10^{-5}$ with an interval of 10^{-4}. Negative contours are dashed. The red squares illustrate, for an example grid point (in red), the observations considered in the local (11×11) grid points region.

Examples of the observations and truths used in the generation

and evaluation of the experiments with data assimilation are displayed in Figure 8. Notice that we run one test with observations of the momentum fields only, and another test with observations of the full set of variables.

The ten ensemble members in each of these tests are initialised with balanced states, and blending is applied for the first time-step when the model runs in the pseudo-incompressible configuration. The ensemble is then solved forward in time with the fully compressible model. Data from the generated observations are assimilated every 25 s. The immediate time-step after the assimilation procedure is solved in the pseudo-incompressible limit regime while the rest of the time-steps in the assimilation window are solved using the fully compressible model. Conversions according to the blending scheme in section 4 are employed when switching back and forth between the full and limit models. Furthermore, the choice of π_{half} is used. The ensemble solved with both data assimilation and blending is abbreviated as EnDAB.

The setup is repeated for two additional ensembles and each observation scenario. One where data are still assimilated but no blending is performed (EnDA), and another where neither data assimilation nor blending are performed (EnNoDA). EnNoDA and EnDA constitute an identical twin experiment [Reich and Cotter, 2015, Lang et al., 2017], through which the effects of data assimilation can be evaluated. EnDA along with EnDAB constitute yet another identical twin experiment, which evaluates the performance of blending.

5.2.2 Rising bubble setup

The rising bubble ensemble spread is generated by randomly modifying the maximum of the potential temperature perturbation $\delta\Theta$ in the open half interval $[2.0\ \text{K}, 12.0\ \text{K})$. The ensemble comprises ten members. While the relative spread of the temperature perturbation is large with this setup, the ensemble spread of the bubble position at the final time of the simulation, $t_{\text{fin}} = 1000.0$ s, is only moderate.

An additional sample is drawn for the obs and the truth, which are identical in this setup. Blending is applied to the first time-step of the obs and the truth, obtaining a balanced solution. As the rising bubble flow fields evolve rather slowly in the beginning, data are only assimilated from $t = 500.0$ s onwards. Observations of the momentum field are then assimilated every 50.0 s. As with the vortex experiments, only a tenth of the grid points are observed, noise with standard deviation 5% of the peak-to-peak amplitude is added, and localisation within an (11×11) grid points region is applied. A

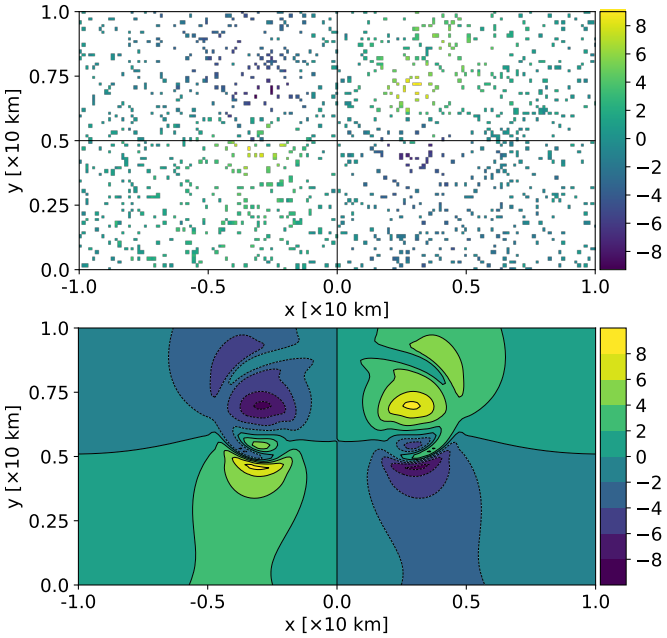

Figure 9: Rising bubble: horizontal momentum field ρu at $t = 1000.0$ s. Sparse and noisy observations (top) and truth (bottom); contours in range $[-8, 8]$ kg m^{-1} s^{-1} with a 2 kg m^{-1} s^{-1} interval, negative contours dashed.

localisation function corresponding to the truncated the Gaussian function is applied and the ensemble is not inflated. Examples of the observation and truth are given in Figure 9. Three ensembles corresponding to the EnNoDA, EnDA, and EnDAB settings, with 10 members each, are generated, but only one set of experiments involving assimilation of the momentum field only is pursued. Note that as the ensembles and the observations are generated with balanced initial conditions, any noise present in the simulation results is the result of the data assimilation procedure.

Table 2 summarises the details of the data assimilation-related experimental setup for both test cases.

5.2.3 Evaluation of data assimilation

The quality of data assimilation is evaluated by a spatially and ensemble averaged root mean square error (RMSE) from the truth.

Table 2: Assimilation-related experimental parameters. K is the ensemble size, b the ensemble inflation factor, t_{first} the first assimilation time, Δt_{obs} the observation interval, $\psi_{\text{assimilated}}$ the set of quantities assimilated, $(N \times N)_{\text{local}}$ the size of the local region, f_{local} the type of localisation function, η_{obs} the observation noise, σ the standard deviation of the Gaussian noise, A the peak-to-peak amplitude of the quantity observed, $\text{obs}_{\text{sparse}}$ the sparsity of the observations, $\Delta t_{\text{blending}}$ the number of initial time-steps spent in the limit model regime. π choice, used in the initialisation of $\Delta t_{\text{blending}}$, is either π_{half} or π_{full}, more details in section 4.3.

Test case		**Vortex**	**Bubble**
Ensemble	K	10 members	
	b	1.0	
Observations	t_{first} [s]	25.0	500.0
	Δt_{obs} [s]	25.0	50.0
	$\psi_{\text{assimilated}}$	$\{\rho u, \rho w\}$ or $\{\rho, \rho u, \rho w, P, \pi\}$	$\{\rho u, \rho w\}$
	$(N \times N)_{\text{local}}$	(11×11) grid points	
	f_{local}	Truncated Gaussian	
	η_{obs}	Gaussian with $\sigma = 0.05A$	
	$\text{obs}_{\text{sparse}}$	One in 10 grid points	
Blending	$\Delta t_{\text{blending}}$	A single blended time-step	
	π choice	π_{half}	

This is given by

$$\text{RMSE}(\psi) = \sqrt{\frac{1}{K}\frac{1}{N_x \times N_z}\sum_{k}^{K}\sum_{i,j}^{N_x,N_z}\left[\psi_k^{\text{ensemble}}(x_i, z_j) - \psi^{\text{truth}}(x_i, z_j)\right]^2}, \quad (54)$$

where $k = 1, \ldots, K$ indexes the ensemble members and $i = 1, \ldots, N_x$ and $j = 1, \ldots, N_z$ the number of grid points in the (x, z) coordinates. ψ is the set of quantities $\{\rho, \rho u, \rho w, P, \pi\}$.

5.3 Ensemble data assimilation and blending: results

5.3.1 Travelling vortex

Figure 10 depicts the ensemble snapshots for the vortex case. EnNoDA (top row) acts as the control ensemble depicting solution of the

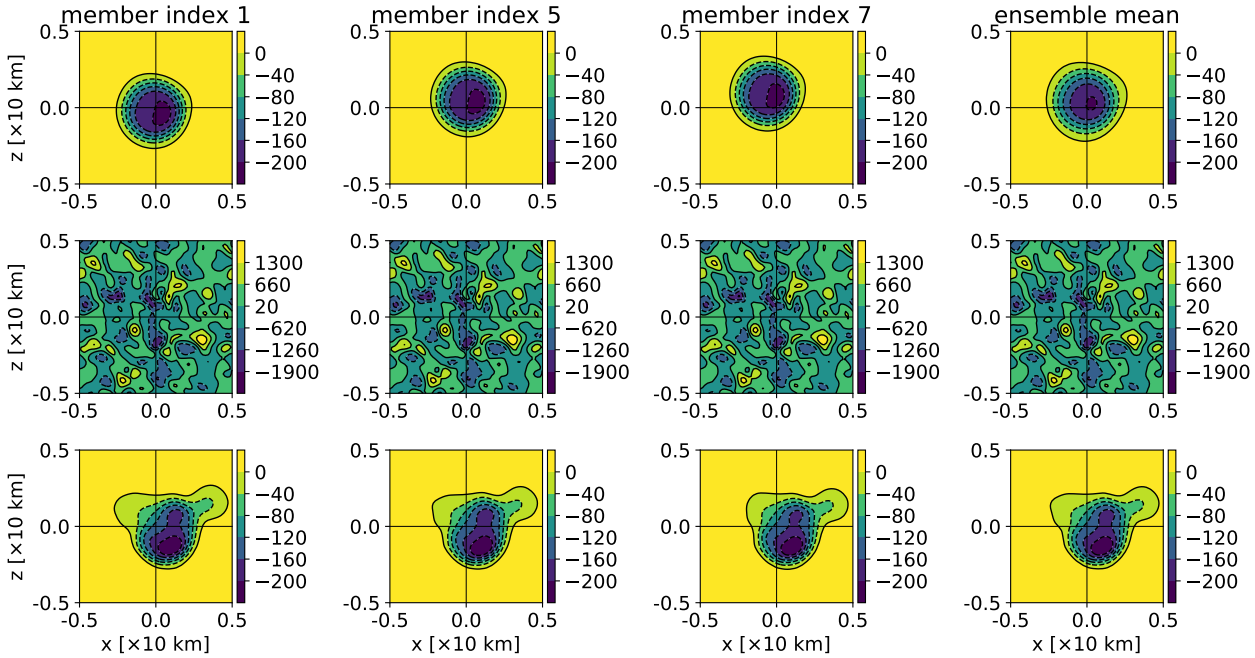

Figure 10: Travelling vortex: snapshots of pressure perturbation p'. Ensemble members with index 1 (first column), 5 (second column), 7 (third column) and ensemble mean (fourth column) at $t = 300.0$ s. Top row: EnNoDA run; contours in range $[-200, 0]$ Pa with a 40 Pa interval. Middle row: EnDA run; contours in range $[-1900, 1300]$ Pa with a 640 Pa interval. Bottom row: EnDAB run; contours in range $[-200, 0]$ Pa with a 40 Pa interval. Negative contours are dashed.

travelling vortex without data assimilation and blending. While the center position of the vortex for each ensemble member is perturbed, the ensemble mean vortex position (fourth column) is centered around the origin. This is in line with the conditions used to generate the initial ensemble. With data assimilation, EnDA (middle row), the balance is lost and at final time the vortex structure is not preserved. Data assimilation and blending, EnDAB (bottom row), recovers the balanced solution and the vortex structure is preserved after three periods of revolution. Moreover, comparing with Figure 8, the effect of data assimilation becomes obvious. The center position of the EnDAB ensemble mean is in the lower right quadrant, closer to that of the observation and the truth.

Assimilating the momentum fields alone is insufficient and the RMSE in the solution (solid lines in Figure 11) is larger than in the reference EnNoDA run. Nevertheless, EnDAB provides a smoother

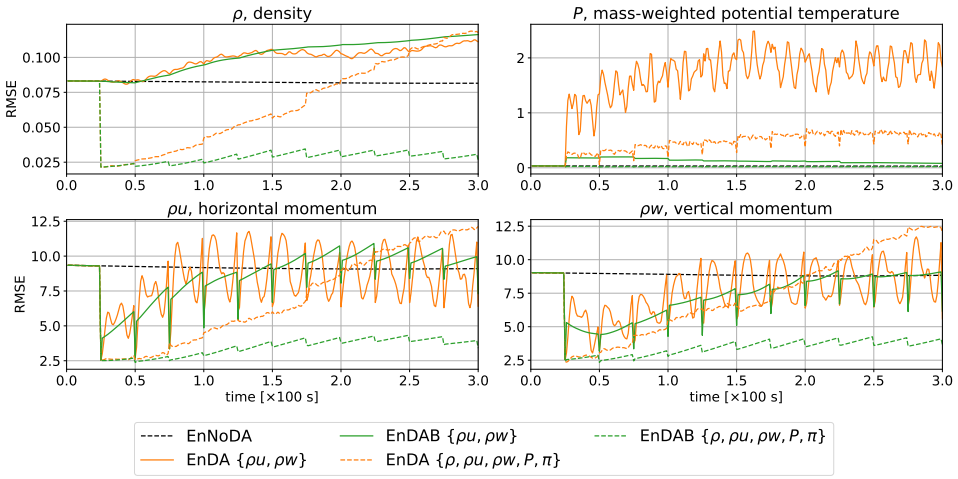

Figure 11: Travelling vortex: EnNoDA run (black), EnDA run (orange), EnDAB run (green). Assimilated quantities are ρu and ρw (solid lines) and $\rho, \rho u, \rho w, P, \pi$ (dashed lines). Spatially and ensemble averaged RMSE from $t = 0.0$s to 300.0s for density ρ (top left, [kg m^{-2}]), mass-weighted potential temperature P (top right, [kPa]), and momenta ρu, ρw (bottom left and right, [kg m^{-1} s^{-1}]). The RMSE of the initial ensemble is omitted.

solution over time as the error does not oscillate. Assimilating all the quantities yields an improvement (dashed lines in Figure 11). For the EnDAB run, the RMSEs are lower than those of the control EnNoDA run for all quantities over the whole simulation.

Assimilating only the momentum fields without blending (EnDA, solid orange line in Figure 11) leads to a jump in the RMSE in the thermodynamic P variable upon the first assimilation at $t = 25$ s. After that, the error stays relatively constant. Appendix B shows that the error jump quantifies the imbalance introduced by the data assimilation procedure.

Assimilation of momentum alone is insufficient in this test, which includes a strong axisymmetric potential temperature variation (Figure 4). The potential temperature is an advected quantity, not corrected by momentum data assimilation. Therefore, the initially tight correlation of the velocity and potential temperature variations gets destroyed in the course of data assimilation. Since the potential temperature is fluid dynamically active through the generation of baroclinic torque, the flow fields of the ensemble members increasingly deviate from their reference as a consequence.

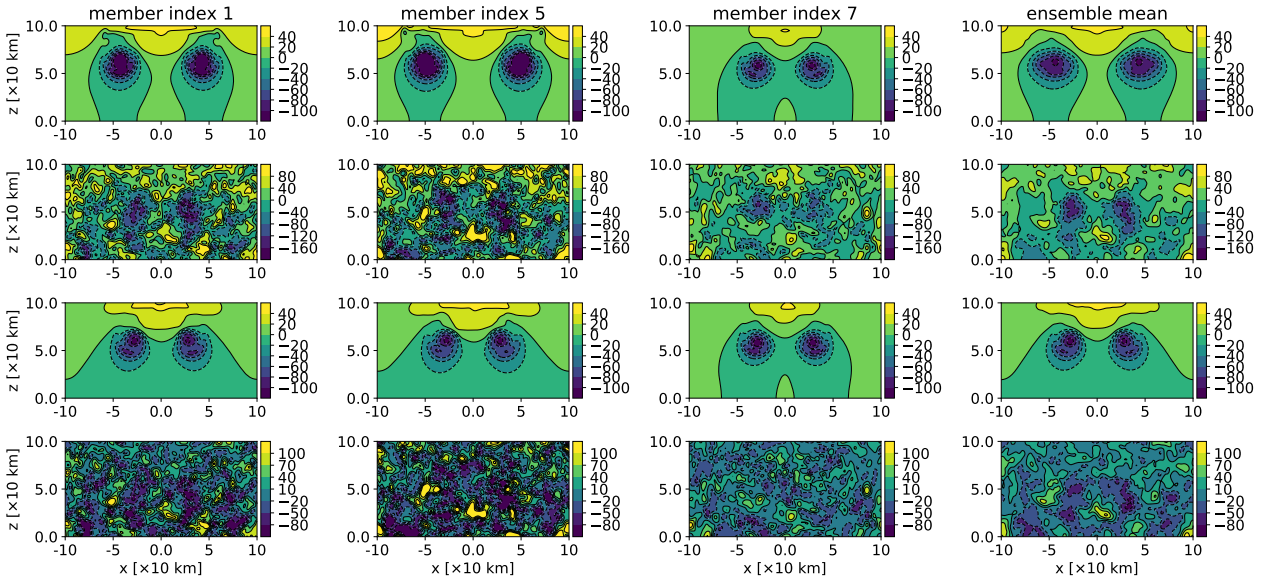

Figure 12: Rising bubble: snapshots of pressure perturbation p'. Ensemble members with index 1 (first column), 5 (second column) and 7 (third column) at $t = 1000.0$ s with the ensemble mean (fourth column). Row-wise: EnNoDA run; contours in range $[-100, 40]$ Pa with a 20 Pa interval (first row), EnDA run; contours in range $[-160, 80]$ Pa with a 40 Pa interval (second row), EnDAB run; contours in range $[-100, 40]$ Pa with a 20 Pa interval (third row), and the difference between EnDA and EnDAB; contours in range $[-80, 100]$ Pa with a 30 Pa interval (fourth row). Negative contours are dashed.

5.3.2 Rising bubble

Figure 12 displays snapshots of pressure perturbation for the bubble case. In the EnNoDA run (first row) the bubbles in the ensemble attain different heights at the end of the simulation time and the ensemble mean is diffused, in line with the spread in the initial conditions used in generating the ensemble. Ensemble members with larger potential temperature perturbation rise faster. In the EnDA ensemble (second row), large-amplitude fast-mode imbalances are present while the ensemble mean shows that the spread of the bubble rotors at the end time converges towards the rotor positions of the truth. For EnDAB (third row), the individual ensemble members are close to one another, as reflected in the ensemble mean. The ensemble converges towards the truth and the fast-mode imbalances are suppressed. Moreover, the bubble rotors are not visible in a plot of the difference between the EnDA and EnDAB ensembles (fourth row), showing that the difference is predominantly due to

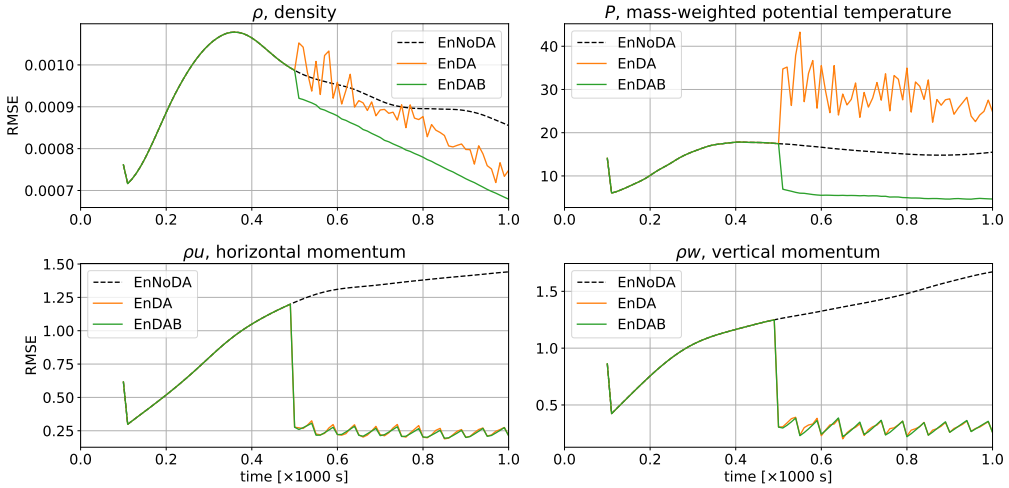

Figure 13: Rising bubble: EnNoDA run (black), EnDA run (orange), EnDAB run (green). Assimilated quantities are ρu and ρw. Spatially and ensemble averaged RMSE from $t = 100.0$ s to 1000.0 s for density ρ (top left, [kg m^{-2}]), mass-weighted potential temperature P (top right, [Pa]), and momenta ρu, ρw (bottom left and right, [kg m^{-1} s^{-1}]).

the presence of the imbalances only, and suggesting (last column) that data assimilation is comparably effective in nudging the bubble towards the truth in both cases.

RMSE plots of data assimilation in the rising bubble experiment are shown in Figure 13. The momentum fields are assimilated every 50.0 s after 500.0 s. This is visible in the momenta RMSE plots, where each downward step corresponds to an assimilation procedure. For EnDA, an error is introduced in the density ρ and mass-weighted potential temperature P. Blending negates this and the EnDAB curves show a smooth profile, with RMSE lower than the control EnDA. As in the travelling vortex case, a jump is visible in the RMSE of P at the first assimilation time. See Appendix B on the scale analysis for more details.

6 Discussion and conclusion

This paper has advanced a new conceptual framework for balanced data assimilation based on blended numerical models. Using a discrete time-level numerical analysis for the Exner pressure field and a careful choice of pressure perturbation variables, the blended soundproof-compressible modelling framework of Benacchio et al. [2014] has been substantially upgraded by a functionality to switch

between equation sets in a single time-step. Numerical results on experiments with imbalanced initial data show that a single time-step in the pseudo-incompressible limit regime is sufficient to recover a balanced state in tests with a travelling vortex and a rising warm air bubble, in which the blended model yielded leftover acoustics with amplitude more than one order of magnitude smaller than the ones generated at the onset with the fully compressible model. The amplitude reduction is a sizeable improvement over the scores of Benacchio et al. [2014] who, in addition, needed several time steps in a hybrid soundproof-compressible configuration with non-integer values of the blending parameter α_P to achieve their best level of noise reduction.

The upgraded blended model has then been combined with a data assimilation engine and deployed as a tool to reduce imbalances introduced by regular assimilation of data within model runs. Numerical results on ensemble data assimilation with blending showed that while data assimilation alone produced imbalances that effectively destroyed solution quality, data assimilation together with blending was able to reduce those imbalances and recover accurate results. In these cases, a single time-step spent in the pseudo-incompressible limit regime after the assimilation of data was again sufficient to restore the balanced state, as highlighted in reduced RMSEs with the blended model.

For ensemble data assimilation experiments with the travelling vortex, assimilation of the momentum fields alone was found to be insufficient. Over longer simulations, the ensemble with balanced data assimilation carried larger errors than the control ensemble without data assimilation. See the green solid curves in Figure 11. We have traced the origin of this result back to an issue of controllability [Jazwinski, 2007]. This test case involves large, dynamically relevant potential temperature variations whose deviation from the truth cannot be reduced (controlled) at all when only the momentum field is assimilated. In fact, a test with an analogous vortex that has constant entropy initial data (not shown) yields results close in quality to those of the rising thermal test when only momentum is assimilated. The issue could then be solved by assimilation of all variables. Further investigation is warranted on how the effectiveness of data assimilation can be improved under such circumstances without the need to observe all state variables. A scale analysis (Appendix B) corroborated the insight that the RMSE increase introduced by the assimilation of data corresponds to the fast-mode imbalances seen in the plots of the individual ensemble members and the ensemble mean.

The results presented in this paper prepare the ground for future work in a number of areas. The effects of blending on balanced local data assimilation can be investigated in tests with stratified background potential temperature, e.g. the ones in Skamarock and Klemp [1994], and on extensions of the method to include support for three-dimensional and moist dynamics [O'Neill and Klein, 2014, Duarte et al., 2015].

The assimilation of vertically integrated observations, such as those obtained by satellite measurements, can be explored within standard test cases as the ones in this paper. Improvements to existing methods can then be sought in a relatively simpler setting.

The quality of data assimilation was evaluated by the root mean square error in this paper. The underlying assumption of a priori knowledge of the truth makes experimental setups deviate from a real-world scenario. A criterion to evaluate the physical consistency of the analysis fields such as the *dynamic state index* [Müller et al., 2018] will allow for the evaluation of the quality of data assimilation in the absence of prior knowledge of the truth, and could also be used to guide balanced data assimilation.

The numerical scheme proposed by Benacchio and Klein [2019] enables solution of the hydrostatic system in the large-scale limit in addition to the small-scale low Mach number limit considered in this paper. Therefore, a blended data assimilation framework such as the one presented here could be enhanced with hydrostatic blending and used in a two-way blended pseudo-incompressible / hydrostatic / compressible model following Klein and Benacchio [2016]. Investigations similar to the ones in this paper can then be made on balancing initial states and data assimilation for small- to planetary-scale dynamics using the resulting doubly blended model. As horizontal resolutions used in global numerical weather prediction models approach the kilometer-scale, operational forecast centres are completing the transition to non-hydrostatic analytical formulations [Kühnlein et al., 2019] while considering the use of reduced models for the dynamics [Voitus et al., 2019]. In this context, multimodel numerics with seamless switching could contribute to creating a level playing field to evaluate accuracy and performance with different equation sets in future dynamical cores. The positive evidence provided here in balancing data assimilation shows, in the authors' view, a considerable potential and potential impact of deploying the blended model framework across the whole forecast model chain.

Acknowledgments R.C., G.H. and R.K. thank the Deutsche Forschungsgemeinschaft for the funding through the Collaborative

Research Center (CRC) 1114 “Scaling cascades in complex systems”, Project Number 235221301, Project A02: “Multiscale data and asymptotic model assimilation for atmospheric flows”. T.B. was supported by the ESCAPE-2 project, European Union’s Horizon 2020 research and innovation programme (grant agreement No 800897).

Appendix A LETKF Algorithm

The Local Ensemble Transform Kalman Filter (LETKF) algorithm presented here is a summary of the algorithm published by Hunt et al. [2007] in their paper, adapted to the blended numerical framework.

Start with an ensemble of K state vectors, $\{\mathbf{x}^f_{k,[g]}\} \in \mathbb{R}^{m_{[g]}}$ for $k = 1, \ldots, K$. Furthermore, assume that a set of observations $\mathbf{y}_{\text{obs},[g]} \in \mathbb{R}^{l_{[g]}}$ with a known covariance $\mathbf{R}_{[g]} \in \mathbb{R}^{l_{[g]} \times l_{[g]}}$ is available. Here, m and l represent the dimension of the state and observation spaces and the subscript $[g]$ represents the global state space, *i.e.* localisation has not been applied.

1. Apply the forward operator $\mathcal{H}$ to obtain the state vectors in the observation space,

$$\mathcal{H}(\mathbf{x}^f_{k,[g]}) = \mathbf{y}^f_{k,[g]} \in \mathbb{R}^{l_{[g]}}. \tag{55}$$

2. Stack the anomaly of the state and observation vectors to form the matrices,

$$\mathbf{X}^f_{[g]} = \left[\mathbf{x}^f_{1,[g]} - \bar{\mathbf{x}}_{[g]} \,|\, \ldots \,|\, \mathbf{x}^f_{K,[g]} - \bar{\mathbf{x}}_{[g]}\right] \in \mathbb{R}^{m_{[g]} \times K}, \tag{56}$$

$$\mathbf{Y}^f_{[g]} = \left[\mathbf{y}^f_{1,[g]} - \bar{\mathbf{y}}_{[g]} \,|\, \ldots \,|\, \mathbf{y}^f_{K,[g]} - \bar{\mathbf{y}}_{[g]}\right] \in \mathbb{R}^{l_{[g]} \times K}, \tag{57}$$

where $\bar{\mathbf{x}}_{[g]}$ ($\bar{\mathbf{y}}_{[g]}$) is the mean of the state vectors (in observation space) over the ensemble, e.g.

$$\bar{\mathbf{x}}_{[g]} = \frac{1}{K} \sum_{k=1}^{K} \mathbf{x}^f_{k,[g]} \in \mathbb{R}^{m_{[g]}}. \tag{58}$$

3. From $\mathbf{X}^f_{[g]}$ and $\mathbf{Y}^f_{[g]}$, select the local $\mathbf{X}^f$ and $\mathbf{Y}^f$.
4. From the global observations $\mathbf{y}_{\text{obs},[g]}$ and observation covariance $\mathbf{R}_{[g]}$, select the corresponding local counterparts $\mathbf{y}_{\text{obs}}$ and $\mathbf{R}$. Notice that the subscript $[g]$ is dropped when representing the local counterparts.
5. Solve the linear system $\mathbf{R}\mathbf{C}^T = \mathbf{Y}^f$ for $\mathbf{C} \in \mathbb{R}^{K\times l}$.
6. Optionally, apply a localisation function to $\mathbf{C}$ to modify the influence of the surrounding observations.
7. Compute the $K \times K$ gain matrix,
$$\mathbf{K} = \left[(K-1)\frac{\mathbf{I}}{b} + \mathbf{C}\mathbf{Y}^f\right]^{-1}, \tag{59}$$
where $b > 1$ is the ensemble inflation factor.
8. Compute the $K \times K$ analysis weight matrix,
$$\mathbf{W}^a = \left[(K-1)\,\mathbf{K}\right]^{1/2}. \tag{60}$$
9. Compute the K-dimension vector encoding the distance of the observations from the forecast ensemble
$$\bar{\mathbf{w}}^a = \mathbf{K}\mathbf{C}\left(\mathbf{y}_{\text{obs}} - \bar{\mathbf{y}}^f\right), \tag{61}$$
and add $\bar{\mathbf{w}}^a$ to each column of $\mathbf{W}^a$ to get a set of K weight vectors $\{\mathbf{w}^a_k\}$ with $k = 1, \ldots, K$.
10. From the set of weight vectors, compute the analysis for each ensemble member,
$$\mathbf{x}^a_k = \mathbf{X}^f\mathbf{w}^a_k + \bar{\mathbf{x}}^f, \quad \text{for } k = 1, \ldots, K. \tag{62}$$
11. Finally, recover the global analysis ensemble $\{\mathbf{x}^a_{k,[g]}\}$, $k = 1, \ldots, K$.
This recovery depends on how the local regions were selected in (56) and (57). For local region surrounding the grid point under analysis, the reassembly of the global analysis ensemble is done by reassembling the analysed grid points back into the global grid.

Appendix B Scale analysis for the data assimilation error in the pressure-related fields

Figures 11 and 13 show that the assimilation of only the momentum fields leads to a jump in RMSE in the non-momentum fields. This

increase in the error occurs after the first assimilation time and remains of the same order of magnitude for the duration of the simulation, quantifying the imbalance introduced by data assimilation. The imbalance can be characterized by a scale analysis [Klein et al., 2001].

The assimilation of the momentum fields leads to a change in the divergence of the velocity fields,

$$\nabla \cdot (\delta \mathbf{v}) = \frac{\partial \delta u}{\partial x} + \frac{\partial \delta w}{\partial z}, \tag{63}$$

where $(\delta u, \delta w)$ are the changes in the velocity fields due to the assimilation of momenta in the vertical slice experiments. (63) has the units $[\mathrm{s}^{-1}]$.

Observe from Figures 10 and 12 that the imbalance introduced by data assimilation are fast-mode acoustic waves. This effect is modelled as a wave oscillating with the peak amplitude right after the assimilation of data at the grid point under analysis. Therefore, for an oscillating wave excited at grid point (x_i, z_j), the maximum amplitude of the imbalances is

$$\begin{aligned}(\nabla \cdot \delta \mathbf{v})_{(i,j)} \int_0^{t_{\mathrm{ac}}} \cos\left(\frac{\pi}{2}\frac{t}{t_{\mathrm{ac}}}\right) dt &= \frac{2t_{\mathrm{ac}}}{\pi}(\nabla \cdot \delta \mathbf{v})_{(i,j)} \left[\int_0^{\pi/2} \cos(\xi) d\xi\right] \\ &= \frac{2t_{\mathrm{ac}}}{\pi}(\nabla \cdot \delta \mathbf{v})_{(i,j)}, \end{aligned} \tag{64}$$

The acoustic timescale t_{ac} is chosen as the timescale of the largest perturbations introduced. This is the time a wave takes to traverse to the edge of the (11×11) grid points local region from the analysis grid point. Therefore,

$$t_{\mathrm{ac}} = \frac{11}{2}\frac{dx}{c_{\mathrm{ref}}}, \tag{65}$$

where dx is the constant grid-size and c_{ref} the speed of sound. (65) has units [s] and (64) is dimensionless.

As $p = \rho c_{\mathrm{ref}}^2$, the contribution to the pressure from $\nabla \cdot (\delta \mathbf{v})_{(i,j)}$ is computed by

$$\frac{2t_{\mathrm{ac}}}{\pi} \nabla \cdot (\delta \mathbf{v})_{(i,j)} \rho_{(i,j)} c_{\mathrm{ref}}^2 \sim \hat{p}_{(i,j)}, \tag{66}$$

which has the units of [Pa]. The hat $\hat{}$ signifies that the quantity is obtained from scale analysis. Finally, use the equation of state (10) to obtain an estimate for $\hat{P}$.

For comparison with the RMSE, the norm is taken for $\hat{P}$, given by

$$\left|\hat{P}\right| = \frac{1}{K}\sum_k^K \left[\sqrt{\frac{1}{N_x \times N_z}\sum_{i,j}^{N_x,N_z}\left(\hat{P}_{(i,j)}\right)^2}\right]_k, \tag{67}$$

where k indexes the K ensemble members and N_x and N_z are the number of grid points in the x and z coordinates.

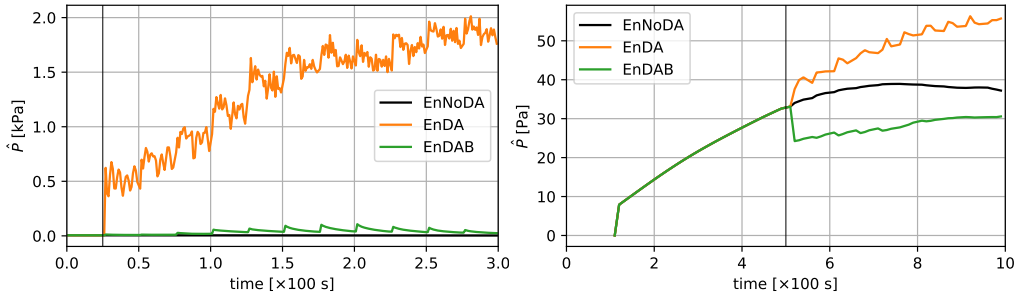

Figure B1: Scale analysis of the contribution to the mass-weighted potential temperature P from the divergence of the velocity fields for the travelling vortex ensemble (left) and the rising bubble ensemble (right). The first assimilation time is marked with a vertical solid black line.

Figure B1 shows the results of scale analysis for the two test cases. Results at assimilation time are omitted. Scale analysis yields EnDA results for $\hat{P}$ that are of the same order of magnitude as the jumps in the RMSE plots (Figures 11 and 13) with a similar profile over time. Scale analysis characterizes the error jump in the thermodynamical RMSE plots as fast-mode imbalances introduced through data assimilation.

References

R. N. Bannister. How is the balance of a forecast ensemble affected by adaptive and nonadaptive localization schemes? *Mon. Wea. Rev.*, 143:3680–3699, 2015. doi: 10.1175/MWR-D-14-00379.1.

T. Benacchio and R. Klein. A semi-implicit compressible model for atmospheric flows with seamless access to soundproof and hydrostatic dynamics. *Mon. Wea. Rev.*, 147:4221–4240, 2019. doi: 10.1175/MWR-D-19-0073.1.

T. Benacchio, W. P. O'Neill, and R. Klein. A blended soundproof-to-compressible numerical model for small-to mesoscale atmospheric dynamics. *Mon. Wea. Rev.*, 142:4416–4438, 2014. doi: 10.1175/MWR-D-13-00384.1.

M. Bocquet. Ensemble Kalman filtering without the intrinsic need for inflation. *Non-linear Processes Geophys.*, 18:735–750, Oct. 2011. doi: 10.5194/npg-18-735-2011.

M. Duarte, A. S. Almgren, and J. B. Bell. A low Mach number model for moist atmospheric flows. *J. Atmos. Sci.*, 72:1605–1620, 2015. doi: 10.1175/JAS-D-14-0248.1.

D. R. Durran. Improving the anelastic approximation. *J. Atmos. Sci.*, 46:1453–1461, 1989. doi: 10.1175/1520-0469(1989)046⟨1453:ITAA⟩2.0.CO;2.

J. Flowerdew. Towards a theory of optimal localisation. *Tellus*, 67A: 25257, 2015. doi: 10.3402/tellusa.v67.25257.

G. Gaspari and S. E. Cohn. Construction of correlation functions in two and three dimensions. *Quart. J. Roy. Meteor. Soc.*, 125: 723–757, 1999. doi: 10.1002/qj.49712555417.

S. J. Greybush, E. Kalnay, T. Miyoshi, K. Ide, and B. R. Hunt. Balance and ensemble Kalman filter localization techniques. *Mon. Wea. Rev.*, 139:511–522, 2011. doi: 10.1175/2010MWR3328.1.

J. Harlim and B. R. Hunt. Local ensemble transform Kalman filter: An efficient scheme for assimilating atmospheric data. Preprints, 2005. `https://www.meto.umd.edu/~ekalnay/pubs/harlim_hunt05.pdf`.

G. Hastermann, M. Reinhardt, R. Klein, and S. Reich. Balanced data assimilation for highly-oscillatory mechanical systems. *arXiv.org*, 2017. `https://arxiv.org/abs/1708.03570`.

C. Hohenegger and C. Schär. Predictability and error growth dynamics in cloud-resolving models. *J. Atmos. Sci.*, 64(12):4467–4478, 2007. doi: 10.1175/2007JAS2143.1.

P. L. Houtekamer and F. Zhang. Review of the ensemble Kalman filter for atmospheric data assimilation. *Mon. Wea. Rev.*, 144: 4489–4532, 2016. doi: 10.1175/MWR-D-15-0440.1.

B. R. Hunt, E. J. Kostelich, and I. Szunyogh. Efficient data assimilation for spatiotemporal chaos: A local ensemble transform Kalman filter. *Physica D*, 230:112–126, 2007. doi: 10.1016/j.physd.2006.11.008.

A. H. Jazwinski. *Stochastic Processes and Filtering Theory*. Dover Publications, 2007.

S. Y. Kadioglu, R. Klein, and M. L. Minion. A fourth-order auxiliary variable projection method for zero-Mach number gas dynamics.

J. Comput. Phys., 227:2012–2043, 2008. doi: 10.1016/j.jcp.2007.10.008.

R. E. Kalman. A new approach to linear filtering and prediction problems. *J. Basic Eng.*, 82:35–45, 03 1960. doi: 10.1115/1.3662552.

J. D. Kepert. Covariance localisation and balance in an ensemble Kalman filter. *Quart. J. Roy. Meteor. Soc.*, 135:1157–1176, 2009. doi: 10.1002/qj.443.

R. Klein. Asymptotics, structure, and integration of sound-proof atmospheric flow equations. *Theor. Comput. Fluid Dyn.*, 23:161–195, 2009. doi: 10.1007/s00162-009-0104-y.

R. Klein. Scale-dependent models for atmospheric flows. *Annu. Rev. Fluid Mech.*, 42:249–274, 2010. doi: 10.1146/annurev-fluid-121108-145537.

R. Klein and T. Benacchio. A doubly blended model for multiscale atmospheric dynamics. *J. Atmos. Sci.*, 73:1179–1186, 2016. doi: 10.1175/JAS-D-15-0323.1.

R. Klein and O. Pauluis. Thermodynamic consistency of a pseudo-incompressible approximation for general equations of state. *J. Atmos. Sci.*, 69:961–968, 2012. doi: 10.1175/JAS-D-11-0110.1.

R. Klein, N. Botta, T. Schneider, C.-D. Munz, S. Roller, A. Meister, L. Hoffmann, and T. Sonar. Asymptotic adaptive methods for multi-scale problems in fluid mechanics. *J. Eng. Math.*, 39:261–343, 2001. doi: 10.1023/A:1004844002437.

R. Klein, S. Vater, E. Päschke, and D. Ruprecht. Multiple scales methods in meteorology. In H. Steinrück, editor, *Asymptotic Methods in Fluid Mechanics: Survey and Recent Advances*, volume 523 of *International Centre for Mechanical Sciences*, pages 127–196. Springer, 2010.

R. Klein, T. Benacchio, and W. O'Neill. Using the sound-proof limit for balanced data initialization. In *Proc. ECMWF Seminar on Numerical Methods*, pages 227–236, Reading, United Kingdom, ECMWF, 2014. available at: https://www.ecmwf.int/sites/default/files/elibrary/2014/10483-using-sound-proof-limit-balanced-data-initialization.pdf.

C. Kühnlein, W. Deconinck, R. Klein, S. Malardel, Z. P. Piotrowski, P. K. Smolarkiewicz, J. Szmelter, and N. P. Wedi. FVM 1.0: A nonhydrostatic finite-volume dynamical core formulation for IFS. *Geosci. Model Dev.*, 12:651–676, 2019. doi: 10.5194/gmd-12-651-2019.

M. Lang, P. Browne, P. J. Van Leeuwen, and M. Owens. Data assimilation in the solar wind: Challenges and first results. *Space Wea.*, 15:1490–1510, 2017. doi: 10.1002/2017SW001681.

A. C. Lorenc. The potential of the ensemble Kalman filter for NWP—A comparison with 4D-Var. *Quart. J. Roy. Meteor. Soc.*, 129:3183–3203, 2003. doi: 10.1256/qj.02.132.

P. Lynch and X.-Y. Huang. Initialization of the HIRLAM model using a digital filter. *Mon. Wea. Rev.*, 120:1019–1034, 1992. doi: 10.1175/1520-0493(1992)120⟨1019:IOTHMU⟩2.0.CO;2.

A. Müller, P. Névir, and R. Klein. Scale dependent analytical investigation of the dynamic state index concerning the quasi-geostrophic theory. *Math. Climate Wea. Forecasting*, 4:1–22, 2018. doi: 10.1515/mcwf-2018-0001.

L. J. Neef, S. M. Polavarapu, and T. G. Shepherd. Four-dimensional data assimilation and balanced dynamics. *J. Atmos. Sci.*, 63: 1840–1858, 2006. doi: 10.1175/JAS3714.1.

W. O'Neill and R. Klein. A moist pseudo-incompressible model. *Atmos. Res.*, 142:133—141, 2014. doi: 10.1016/j.atmosres.2013.08.004.

J. Pedlosky. *Geophysical Fluid Dynamics*. Springer, 2 edition, 2013.

S. Reich and C. J. Cotter. Ensemble filter techniques for intermittent data assimilation. In S. K. Mike Cullen, Melina A Freitag and R. Scheichl, editors, *Large Scale Inverse Problems: Computational Methods and Applications in the Earth Sciences*, volume 13 of *Radon Series on Computational and Applied Mathematics*, pages 91–134. De Gruyter, 2013.

S. Reich and C. J. Cotter. *Probabilistic Forecasting and Bayesian Data Assimilation*. Cambridge University Press, 2015.

W. C. Skamarock and J. B. Klemp. Efficiency and accuracy of the Klemp-Wilhelmson time-splitting technique. *Mon. Wea. Rev.*, 122:2623–2630, 1994. doi: 10.1175/1520-0493(1994)122⟨2623:EAAOTK⟩2.0.CO;2.

P. K. Smolarkiewicz. On forward-in-time differencing for fluids. *Mon. Wea. Rev.*, 119:2505–2510, 1991. doi: 10.1175/1520-0493(1991)119⟨2505:OFITDF⟩2.0.CO;2.

P. K. Smolarkiewicz and A. Dörnbrack. Conservative integrals of adiabatic Durran's equations. *Int. J. Numer. Methods Fluids*, 56: 1513–1519, 2008. doi: 10.1002/fld.1601.

P. K. Smolarkiewicz and L. O. Margolin. On forward-in-time differencing for fluids: Extension to a curvilinear framework. *Mon. Wea. Rev.*, 121:1847–1859, 1993. doi: 10.1175/1520-0493(1993)121⟨1847:OFITDF⟩2.0.CO;2.

P. K. Smolarkiewicz, C. Kühnlein, and N. P. Wedi. A consistent framework for discrete integrations of soundproof and compressible PDEs of atmospheric dynamics. *J. Comput. Phys.*, 263:185–205, 2014. doi: 10.1016/j.jcp.2014.01.031.

G. K. Vallis. *Atmospheric and Oceanic Fluid Dynamics: Fundamentals and Large-Scale Circulation*. Cambridge University Press, 2 edition, 2017.

P. J. Van Leeuwen, Y. Cheng, and S. Reich. *Nonlinear Data Assimilation*. Springer, 2015.

F. Voitus, P. Bénard, C. Kühnlein, and N. P. Wedi. Semi-implicit integration of the unified equations in a mass-based coordinate: model formulation and numerical testing. *Q. J. R. Meteorol. Soc.*, 145(725):3387–3408, 2019. doi: 10.1002/qj.3626.

C. K. Wikle and L. M. Berliner. A Bayesian tutorial for data assimilation. *Physica D*, 230:1–16, 2007. doi: 10.1016/j.physd.2006.09.017.

M. Zupanski. Theoretical and practical issues of ensemble data assimilation in weather and climate. In S. K. Park and L. Xu, editors, *Data Assimilation for Atmospheric, Oceanic and Hydrologic Applications*, volume 1, pages 67–84. Springer, 2009.

MOX Technical Reports, last issues

Dipartimento di Matematica
Politecnico di Milano, Via Bonardi 9 - 20133 Milano (Italy)

16/2021 Salvador, M.; Dede', L.; Manzoni, A.
Non intrusive reduced order modeling of parametrized PDEs by kernel POD and neural networks

13/2021 Ferro, N.; Perotto, S.; Cangiani, A.
An anisotropic recovery-based error estimator for adaptive discontinuous Galerkin methods

14/2021 Peli, R.; Menafoglio, A.; Cervino, M.; Dovera, L.; Secchi, P;
Physics-based Residual Kriging for dynamically evolving functional random fields

15/2021 Fumagalli, A.; Patacchini, F.S.
Model adaptation in a discrete fracture network: existence of solutions and numerical strategies

10/2021 Di Michele, F.; May, J.; Pera, D.; Kastelic, V.; Carafa, M.; Smerzini, C.; Mazzieri, I.; Rubino,
Spectral elements numerical simulation of the 2009 L'Aquila earthquake on a detailed reconstructed domain

11/2021 Antonietti,P.F.; Manzini, G.; Mazzieri, I.; Scacchi, S.; Verani, M.
The conforming virtual element method for polyharmonic and elastodynamics problems: a review

12/2021 di Cristofaro, D.; Galimberti, C.; Bianchi, D.; Ferrante, R.; Ferro, N.; Mannisi, M.; Perotto, S
Adaptive topology optimization for innovative 3D printed metamaterials

09/2021 Riccobelli, D.; Noselli, G.; DeSimone, A.
Rods coiling about a rigid constraint: Helices and perversions

08/2021 Antonietti, P. F.; Manuzzi, E.
Refinement of polygonal grids using Convolutional Neural Networks with applications to polygonal Discontinous Galerkin and Virtual Element methods

07/2021 Diquigiovanni, J.; Fontana, M.; Vantini, S.
The Importance of Being a Band: Finite-Sample Exact Distribution-Free Prediction Sets for Functional Data